

NASA Technical Paper 1217

Space Shuttle Active-Pogo-  
Suppressor Control Design  
Using Linear Quadratic  
Regulator Techniques

Bruce Lehtinen and Carl F. Lorenzo

JANUARY 1979

**NASA**

COPY FILE  
COPY

NASA Technical Paper 1217

Space Shuttle Active-Pogo-  
Suppressor Control Design  
Using Linear Quadratic  
Regulator Techniques

Bruce Lehtinen and Carl F. Lorenzo  
*Lewis Research Center  
Cleveland, Ohio*

**NASA**

National Aeronautics  
and Space Administration

**Scientific and Technical  
Information Office**

1979

## CONTENTS

	Page
SUMMARY . . . . .	1
INTRODUCTION . . . . .	1
POGO SYSTEM MODEL . . . . .	2
Overall Model Structure . . . . .	2
Controls and Measurements . . . . .	3
State-Variable System Model . . . . .	3
Worst-Case-Model Parameter Selection . . . . .	5
System Eigenvalues . . . . .	6
System Frequency Responses . . . . .	6
Active-Pogo-Suppressor-Control Design Philosophy . . . . .	6
LINEAR QUADRATIC REGULATOR THEORY . . . . .	7
MINIMUM ROOT-MEAN-SQUARE (rms) DESIGN . . . . .	9
Full-State Feedback . . . . .	10
Kalman Filter Feedback . . . . .	11
Frequency-Domain Interpretation of Kalman Filter Feedback . . . . .	12
Non-Minimum-Phase Controllers . . . . .	14
Partial-State-Feedback Minimum-rms Control Designs . . . . .	15
MODAL CONTROL APPROACH TO SUPPRESSOR CONTROL DESIGN . . . . .	17
Performance Index Formulation . . . . .	17
Full-State Feedback . . . . .	20
Sensitivity of Full-State Feedback Designs . . . . .	21
Partial-State Feedback . . . . .	22
Generation of Unmeasurable Modal State Variables . . . . .	22
Mode-Shape Analysis of Partial-State Feedback Design . . . . .	25
Sensitivity of Partial-State Feedback Designs . . . . .	25
Comparison of Modal Control and Minimum-rms Designs . . . . .	26
Frequency-Domain Behavior of Modal Control Designs . . . . .	27
Use of Kalman Filter with Modal Control Designs . . . . .	27
CONCLUSIONS . . . . .	28
APPENDIXES	
A - SYMBOLS . . . . .	30
B - STATE-VARIABLE SPACE SHUTTLE POGO MODEL . . . . .	34
C - LISTING OF SUBROUTINE POGMAT . . . . .	46
REFERENCES . . . . .	53

## SUMMARY

Two methods of active pogo suppression (stabilization) for the space shuttle vehicle were studied analytically. The basis for both approaches was the linear quadratic regulator, state space technique. The first approach minimized root-mean-square pump inlet pressure by using either full-state feedback, partial-state feedback, or output feedback with a Kalman filter. The second approach increased the modal damping associated with the critical structural modes by using either full-state feedback or reconstructed-state feedback.

A number of implementable controls were found by both approaches. The designs were analyzed with respect to sensitivity, complexity, and controller energy requirements, as well as controller performance. Practical controllers resulting from the two design approaches tended to use pressure and flow as feedback variables for the minimum-rms method and structural accelerations or velocities for the modal control method. Both approaches are suitable for the design of active pogo-suppression controllers.

## INTRODUCTION

The problem of coupled feed-system - structural instabilities of booster vehicles (known as pogo) has persisted from early boosters to present vehicles. The classical approach to solving the problem has been to place accumulators on the suction side of the feed pumps. These accumulators, in general, have been tuned to be most absorbent at the offending feed-system - structural frequency. Efforts have been made to expand the effective frequency range of such accumulators. As a generality, unless these devices are purely compliant (usually adding to existing pump inlet compliance), they introduce additional resonant modes to the feed system. These added modes can in turn couple with the structure to create new instabilities.

In recent years, an attempt has been made to stabilize pogo by adding an active suppressor or controller to the feed system (ref. 1). By such an approach the suppressor response could be tailored to the required response over the bandwidth of the servo, and system flexibility could be improved. Farrell and Fenwick (ref. 1) began this approach by demonstrating an active suppression system experimentally on a test-stand, liquid-oxygen system. Then Lock and Rubin (ref. 2) considered the application

of various suppression system designs to the space shuttle vehicle system. Seidel, Lorenzo, and Lehtinen (ref. 3) used the Lock-Rubin shuttle pogo model to study the problem of control-system design by using frequency-domain optimization techniques.

In this report, time-domain optimization techniques and, again, the Lock-Rubin shuttle pogo model are used to design an active pogo suppressor. Two approaches are examined, both based on linear quadratic regulator theory: The first is called the minimum-rms design approach, and the second is called the modal control design approach. The objective in the minimum-rms design approach is to minimize the root-mean-square value of the high-pressure-oxidizer-pump (HPOP) suction pressure variations in response to a flow-rate disturbance at the HPOP inlet. Two variations of this approach were studied: (1) feedback of HPOP suction pressure through a Kalman filter and (2) partial-state feedback of selected variables (including HPOP suction pressure) resulting in a suboptimal design. In the modal control design approach, the objective is to maximize the eigenvalue damping associated with critical structural pogo modes by feedback of reconstructed modal state information. The sensors required for this purpose are a few selected vehicle accelerometers.

The body of the report comprises three major sections. In the first, the development of a suitable system model and the controller design philosophy are discussed. A short review of linear quadratic regulator theory is presented next, followed by the second main section, which discusses the minimum-rms design approach. And finally, the modal control design approach is presented. An appendix describes the formulation of the space shuttle, state-variable pogo model, upon which the designs discussed in the report are based.

## POGO SYSTEM MODEL

The space shuttle system configuration that was used for analysis and design of the active pogo suppressor is shown in figure 1. As in previous studies (ref. 4), only the liquid-oxygen side of the feed system is considered in the analysis.

### Overall Model Structure

The liquid-oxygen tank is located forward in the main vehicle (fig. 1(a)) and is connected to the engines through a 31.1-meter-long duct running alongside the main tank. This duct is represented in figure 1(b) by the portion between stations 1 and 2. (A more detailed schematic is shown in fig. 26.) The duct is followed by an elbow connected to an 8.47-meter-long crossover duct (stations 2 to 3) that feeds the low-pressure oxidizer pump (LPOP). The LPOP in turn feeds the HPOP through a short

interpump duct (between stations 5 and 7). It is at the inlet to the HPOP that the suppressor's piston actuator is assumed to be located. The HPOP exhausts the liquid oxygen through a short discharge duct into the engine thrust chamber. This simplified liquid-oxygen-system configuration is the same as the configuration used in references 2 to 4. For instance, one major simplification is that the three shuttle main engines and their associated discharge ducts are modeled as a single engine of equivalent thrust. A more detailed development of this model is contained in appendix B. (Symbols are defined in appendix A.)

As in reference 3, the model used for this study contains seven liquid-oxygen-system structural elements that can move independently of one another. These elements are the liquid-oxygen tank, the two feedline segments, the two elbows, the LPOP, and the interpump duct - HPOP - discharge line - thrust chamber combination. The propulsion system dynamics are characterized by flow rates and pressures throughout the system.

### Controls and Measurements

Pogo oscillation is to be suppressed by means of an electrohydraulic piston actuator, at the HPOP inlet, that can insert or extract flow from the interpump duct so as to have an overall stabilizing effect on the system. This study assumes that measurements available to be fed back to the actuator are flows and pressures within the liquid-oxygen system and the accelerations of any of the aforementioned seven system structural elements.

### State-Variable System Model

Because a state-variable model of the pogo system had to be used in applying linear quadratic regulator techniques, some modifications had to be made to the model discussed in reference 4. As shown in appendix B, the main modification was to formulate the line dynamics as a lumped- instead of a distributed-parameter model. Once this was done, the remainder of the task was simply to reformulate the set of ordinary differential equations into the standard state-variable form

$$\dot{x} = Ax + Bu + Dw \tag{1}$$

$$y = Hx \tag{2}$$

The details of this manipulation are given in appendix B.

Figure 2 shows schematically how the state-variable model is structured. Three main portions make up the overall model. Each portion has state variables associated with it. These state variables then comprise the overall system state vector  $x$ .

The propulsion-system-dynamics block in figure 2 contains flow and pressure relationships for the tank, pumps, lines, and engine. Coupled to it is the suppressor actuator, which is assumed to have first-order dynamics. Actuator input voltage  $u_a$  will induce a change in actuator piston velocity and thereby produce a change in the injected flow rate  $Q_a$ . The vector  $x_p$  shown in the figure is the propulsion system state vector and consists of the following 29 states:

$$x_p^T \triangleq (\bar{q}_1, p_1, \bar{q}_2, p_2, \bar{q}_3, p_3, \bar{q}_4, p_4, \bar{q}_5, p_5, \bar{q}_6, p_6, \bar{q}_7, p_7, \\ \bar{q}_8, p_8, Q_1, p_1, Q_2, p_{10}, \bar{q}_{11}, p_{11}, Q_4, p_4, Q_5, p_7, Q_{tc}, Q_a)$$

The capital  $Q$ 's and  $P$ 's are flows and pressures at stations indicated in figure 26. The lower-case  $\bar{q}$ 's and  $p$ 's correspond to flows and pressures at discretely spaced points (lumps) along the first and second feedlines and reflect the lumped-parameter modeling process. This notation was chosen to be consistent with references 2 to 4. The variable  $Q_a$  is the flow supplied by the actuator.

The structural-dynamics block in figure 2 contains the modal structural dynamic relationships. A six-mode structural model was selected for this study. Although other studies (ref. 4) used one-mode-at-a-time analyses, we felt that it would be more advantageous to include the six predominant structural modes simultaneously in the model. In this way, control designs based on this model automatically take into account any possible modal interactions. The state variables most convenient for analysis were chosen. They are the generalized modal displacements  $q$  and velocities  $\dot{q}$ . Thus, the 12th-order vector of structural states is defined as

$$x_s^T \triangleq (q_1, \dot{q}_1, q_2, \dot{q}_2, \dots, q_6, \dot{q}_6)$$

Because the vector  $x_s$  (unlike  $x_p$ ) is unmeasurable, it is important that the model include structural variables that are measurable for use as feedback variables. The following 12 measurable structural variables are defined as the structural output vector  $y_s$ :

$$y_s^T \triangleq (\dot{x}_{l1}, \dot{x}_1, \dot{x}_3, \dot{x}_4, \dot{x}_7, \dot{x}_{tb}, \dot{z}_{l2}, \dot{z}_1, \dot{z}_3, \dot{z}_4, \dot{z}_7, P_{tb})$$

Here, subscripts  $l1$  and  $l2$  refer to the first and second feedlines. For convenience, tank pressure  $P_{tb}$  is considered as a structural output.

In judging the effectiveness of an active suppression system, and in designing controls that use reasonable amounts of control power, it is important to determine a suitable model for external system disturbances. For this study, the main disturbance considered was a random noise signal that resulted in a flow-rate disturbance  $Q_{d7}$  at the HPOP inlet. This disturbance is denoted by the signal  $w_{cn}$  in figure 2 and is modeled by passing white noise through a 100-hertz, second-order filter with 0.707 damping. (See appendix B for details.) This modeling introduces two additional noise states, or  $x_{cn} \triangleq (x_{cn1}, x_{cn2})$ , where  $x_{cn1} \triangleq w_{cn}$ .

Thus, the overall 43rd-order state vector  $x$  is

$$x^T \triangleq \left( x_p^T \mid x_s^T \mid x_{cn}^T \right)$$

where the propulsion states  $x_p$  as well as the structural outputs  $y_s$  are measurable. The elements in matrices A, B, D, and H are computed by subroutine POGMAT (appendix C).

#### Worst-Case-Model Parameter Selection

Because the data (ref. 4) defining the model are preliminary and some model parameters vary considerably over a flight, some method of handling parameter uncertainty had to be included in the control design process. We decided to select critical parameters so as to achieve a worst-case model. Worst case was defined as the model that was least stable in the open loop. The propulsion system parameters that most depend on flight condition are pump inlet bubble compliances  $C_{b1}$  and  $C_{b2}$  and pump gains  $m_1 + 1$  and  $m_2 + 1$ . Ranges for these variables are shown in table I. Structural system parameters that are required to define the model are mainly modal vector data, modal frequencies, masses, and damping ratios. These quantities are given in table II (also see ref. 4) for the two flight conditions of interest (least stable) - end burn and after solid-rocket separation.

From preliminary stability (eigenvalue) calculations on the system A matrix, the sixth structural mode (27.2 Hz) was the least stable mode for end burn in the frequency range of primary interest (<30 Hz) for the overall coupled system. The 2.30-hertz mode was least stable for the after-separation condition. Therefore, the end-burn structural mode at 2.81 hertz (E1 in table II) was replaced by the 2.30-hertz mode from the after-separation condition. The frequency of the sixth end-burn mode was lowered to 24 hertz, a condition that made for an unstable overall system mode at 23.8 hertz. Also, the pump gains were set to their maximum values and the bubble compliances were set to their minimum values (table I).

## System Eigenvalues

The eigenvalues of the A matrix for this worst-case model are shown in figure 3. The six modes primarily associated with the six structural modes of the uncoupled structural system are denoted by the solid symbols. The frequencies of these modes have not shifted appreciably from the original structural modal frequencies. However, the damping ratios for these modes have almost all decreased from their original value of 0.01. In fact, the mode at 23.8 hertz is unstable. Throughout this study, primary interest is focused on the 13 modes that occur at frequencies less than 30 hertz. There are seven somewhat lightly damped modes between 30 and 50 hertz that are associated with line dynamics. However, they are not affected by control or parameter variations and are included in the model mainly to provide better model accuracy at low frequencies. Three real poles are present: one for the actuator, one associated with the interpump duct, and one very high-frequency pole associated with the thrust chamber. Also present is the 100-hertz noise-coloring mode.

## System Frequency Responses

To fully characterize the worst-case system model in the frequency domain would require a number of frequency-response plots equal to the number of system outputs, which could be as high as 41. However, the stability characteristics can be observed by examining the plot of a key measurement variable, namely, HPOP inlet pressure  $P_7$ . Figure 4 is a frequency-response plot of  $P_7$  to disturbance flow  $Q_{d7}$  at the HPOP inlet. In this and all subsequent plots, pressures and flow rates are normalized and phase angles are usually principal values. The plotting resolution is 0.1 hertz. Pressures are normalized to the nominal average value of thrust chamber pressure - taken as  $2.07 \times 10^7$  pascals (3000 psi). Flows are normalized to the nominal average value of total liquid-oxygen flow rate - taken as  $3.52 \times 10^5$  cm<sup>3</sup>/sec (21 500 in<sup>3</sup>/sec). There are six main resonant peaks, all less than 25 hertz. The highest resonance occurs near the 2.3-hertz, lightly damped, after-separation mode; and the second highest occurs near the unstable, 23.8-hertz mode. The presence of the unstable mode is evident in the phase angle plot, where there is a large phase lead near 24 hertz.

## Active-Pogo-Suppressor-Control Design Philosophy

Figures 3 and 4 illustrate the pogo instability problem from two viewpoints - the modal viewpoint and the system-response viewpoint. In the modal viewpoint, demonstrated in figure 3, the primary means of evaluating stability is to examine modal

damping ratios. It has been found desirable in the past to have predominant system modal damping ratios all greater than 0.01 in order to have acceptable overall system performance. This is not the case here. Five modes in the less-than-30-hertz region have damping ratios less than 0.01, and of course one mode is unstable. The control design philosophy stemming from the modal viewpoint is this: Design a controller that will cause the damping ratios of all predominant modes to be greater than 0.01 with the restriction that the frequency of modes associated with actuator motion be less than some prescribed value. This restriction indirectly assures that the design be implementable with an actuator that consumes a reasonable amount of power.

In the system-response viewpoint, on the other hand, the primary concern is to minimize, in some sense, the response of critical system variables to outside disturbances and at the same time to minimize the amount of actuator power required for control. Of course in minimizing system response, the control must, at least, stabilize the system. For the pogo problem, figure 4 illustrates a key system variable response to the main disturbance of interest,  $\tilde{Q}_{d7}$ . The objective of a pogo suppressor designed from the system-response viewpoint is to reduce the resonant peaks of this response and to "quiet" the HPOP inlet pressure and, by doing so, to stabilize the overall system. This design approach requires that the actuator output response in the closed loop be computed to assess whether an excessive amount of control power is required.

Both design viewpoints are discussed in the report. Although each has its advantages and disadvantages, either approach can be used to obtain a suitable suppressor design.

## LINEAR QUADRATIC REGULATOR THEORY

Both approaches to suppressor design discussed in the previous section are implemented by using linear quadratic regulator (LQR) techniques. This section summarizes the main aspects of LQR and Kalman filter theory used in these design approaches.

The linear, time-invariant plant to be controlled can be described by the state equations

$$\dot{x} = Ax + Bu + Dw \quad (3)$$

$$y = Hx + v \quad (4)$$

where  $w$  and  $v$  are white Gaussian plant and measurement noise vectors. The correlations for these noises are

$$E\{w(t)w(t + \tau)^T\} = \psi_w \delta(\tau) \quad (5)$$

$$E\{v(t)v(t + \tau)^T\} = \psi_v \delta(\tau) \quad (6)$$

where  $\psi_w$  and  $\psi_v$  are power spectral density (PSD) matrices.

The problem is to find a control  $u$  that minimizes a quadratic performance index

$$J = E\{x^T R_1 x + u^T R_2 u\} \quad (7)$$

where  $R_1$  and  $R_2$  are, respectively, positive semidefinite and positive definite symmetric weighting matrices. The solution to this problem is the so-called linear quadratic regulator (LQR). If the state vector  $x$  is measurable, the resulting control law is

$$u = -K_c x \quad (8)$$

where the control gain matrix  $K_c$  is

$$K_c = R_2^{-1} B^T S \quad (9)$$

and  $S$  is the solution to the Riccati equation

$$SA + A^T S - SBR_2^{-1}B^T S + R_1 = 0 \quad (10)$$

Figure 5 shows the structure for the LQR solution with full-state feedback. The Riccati solution for obtaining feedback gains  $K_c$  can be obtained with existing computer programs (ref. 5).

If only the measurement  $y$  is available but not the complete state vector  $x$ , an optimal estimate  $\hat{x}$  of the state is required. This estimate can be obtained by using a Kalman filter, described by

$$\dot{\hat{x}} = A\hat{x} + Bu + K_e(y - Hx) \quad (11)$$

where the Kalman gain matrix is given as

$$K_e = PH^T \psi_v^{-1} \quad (12)$$

and where  $P$ , the covariance of the estimation error  $e = \hat{x} - x$ , is the solution to the Riccati equation

$$AP + PA^T - PH^T \psi_v^{-1} HP + D\psi_w D^T = 0 \quad (13)$$

Figure 6 shows the structure for the LQR solution when a Kalman filter is used in the feedback loop. Note that control gains  $K_c$  multiply  $\hat{x}$ , instead of  $x$  as in full-state feedback.

Information on control system performance can be obtained by computing  $X$ , the state covariance matrix, a matrix whose diagonal elements are the mean-square values of the system states. When a Kalman filter is used, the covariance matrix  $X$  can be obtained by solving the Lyapunov equation

$$(A - BK_c)X + X(A - BK_c)^T + (BK_c)P + P(BK_c)^T + D\psi_w D^T = 0 \quad (14)$$

This equation can also be used with full-state feedback. For this case,  $P = 0$  and the equation again can be solved for the covariance matrix  $X$ .

Information on closed-loop system stability with full-state feedback can be obtained by getting the eigenvalues of  $A - BK_c$ . When the Kalman filter is used, stability is described by the eigenvalues of  $A - BK_c$  plus the eigenvalues of  $A - K_c H$ . These eigenvalues are automatically calculated if a Riccati program of the type appearing in reference 5 is used in computing the linear quadratic regulator and Kalman filter gains.

#### MINIMUM ROOT-MEAN-SQUARE (rms) DESIGN

The first of the LQR-based suppressor design methods to be discussed is designated the "minimum-rms design" approach. As the name indicates, the stated objective of this method is to minimize the rms value of the HPOP suction pressure  $P_7$  to disturbance  $Q_{d7}$  (flow-rate perturbation at the HPOP inlet). This objective can be achieved by minimizing mean-square values. Mathematically, the objective is represented as

$$\text{Minimize } J_R = E \left\{ P_7^2 + r_2 u_a^2 \right\} \quad (15)$$

Here, a penalty has been placed on commanded suppressor flow  $u_a$  so as to limit the amount of control flow used by the suppressor. Standard performance-index weighting matrices  $R_1$  and  $R_2$  can then be written as

$$R_1 = \text{diag}(0, 0, \dots, 1; 0, \dots, 0) \quad (16)$$

26

$$R_2 = r_2 \quad (17)$$

## Full-State Feedback

So that baseline suppressor designs could be determined, a series of LQR solutions were run on the assumption that the full 43rd-order state vector was available for feedback. A number of runs were made with various values of  $r_2$ . The computer program of reference 5 was used to solve the Riccati equation. For large values of  $r_2$ , control gains  $K_c$  and system eigenvalue damping ratios were small. For all values of  $r_2$  the closed-loop system was stable, as predicted by theory.

The open- and closed-loop behavior of one particular design case is shown in figure 7(a). Here the open- and closed-loop frequency-response magnitudes for  $P_7$  responding to disturbance  $Q_{d7}$  are compared. In addition to stabilizing the system, state feedback has greatly attenuated the frequency-response magnitude peaks in the frequency range 0 to 30 hertz. Nowhere does the closed-loop response exceed the open-loop response.

The response of commanded suppressor flow  $\tilde{u}_a$  to disturbance  $\tilde{Q}_{d7}$  is shown in figure 7(b). Much of the control effort is, as would be expected, concentrated at the locations of the resonant peaks in the  $\tilde{P}_7/\tilde{Q}_{d7}$  response. The response amplitude is smallest at the points where minimums occur in the  $\tilde{P}_7$  response. Thus, in minimizing performance index  $J_R$ , no real benefit is obtained by further reducing low-amplitude portions of the  $\tilde{P}_7$  response. The maximum in figure 7(b) occurs near the 24-hertz peak in the  $\tilde{P}_7/\tilde{Q}_{d7}$  response, not near the 2.3-hertz peak. The reason is that the 24-hertz peak corresponds to an unstable open-loop mode but the 2.3-hertz peak corresponds to a very lightly damped but stable mode. Thus, the control works hardest in mode stabilization.

It is more informative to examine, for full-state feedback designs, the trade-off between control effort and resultant rms values of  $\tilde{P}_7$ . For this evaluation, the mean-square system response was calculated for a number of designs. Each design corresponded to a different control weighting  $r_2$ . All designs are optimal for any rms level of disturbance  $\tilde{Q}_{d7}$ . In figure 8, results are presented for an assumed rms value for  $\tilde{Q}_{d7}$  ( $\tilde{\sigma}_{Q_{d7}}$ ) of 10 percent. For larger allowable rms suppressor flows, the rms value of HPOP suction pressure decreases. Although not shown in the figure,  $\tilde{\sigma}_{P_7}$  goes to infinity as rms suppressor flow is decreased to zero because the system is open-loop unstable. Hence without a stabilizing control, the rms value of  $\tilde{P}_7$  would be infinite.

Another point to be noted in figure 8 is that the curve is asymptotic to a normalized suppressor flow of 10 percent, which is equal to the rms value of the disturbance. Thus, if a suppressor is available with a capacity approaching the rms disturbance flow, large attenuations in HPOP suction pressure can be achieved. This is, however, generally not the case. For example, a reasonably sized actuator may have a 15.2-

centimeter- (6-in.-) diameter piston with a maximum slewing rate of 254 cm/sec (100 in/sec), for a maximum flow rate of 46 900 cm<sup>3</sup>/sec (2860 in<sup>3</sup>/sec). If this is the 3 $\sigma$  limit, the allowable rms suppressor flow would be 15 700 cm<sup>3</sup>/sec (956 in<sup>3</sup>/sec), or (normalized) 4.5 percent of the nominal liquid-oxygen flow. From figure 8 the resultant normalized rms suction pressure would be about 1.9 percent.

Figure 8 represents an idealized situation, that is, full-state feedback and no measurement noise. Such designs are obviously impractical to implement without some simplification. One approach is to eliminate those feedback gains that least affect performance. This approach is not always possible; but, as in the section Partial-State-Feedback Minimum-rms Control Designs, reasonably simple state feedback designs can be achieved for the problem considered here. A second approach is to use only a few measurements of the most easily sensed variables and to estimate the unmeasurable state variables by using a Kalman filter. This approach is discussed next.

### Kalman Filter Feedback

Numerous measurement configurations can be used with a Kalman filter. Many considerations are involved in the choice of measurements - for example, sensor cost, accuracy, reliability, and noise levels. For the pogo problem, we decided to consider the simplest possible case, namely, a single sensor. The sensed variable chosen was P<sub>7</sub>, a variable that has been shown in other investigations (refs. 3 and 4) to be a key feedback variable.

A number of Kalman filters were designed that used P<sub>7</sub> as a single noisy measurement. Each design corresponded to a different assumed level of measurement noise. The loop was closed around the filter by using the same sets of optimal control gains discussed in the previous section. The overall control loop is depicted in figure 6. The results are plotted at discrete points and are connected by straight lines. The set of resultant design trade-offs can be displayed in an rms value plot, as shown in figure 9. This figure, as does figure 8, shows normalized rms HPOP suction pressure as a function of normalized rms suppressor flow for a normalized rms disturbance flow of 10 percent. The rms values were obtained by solving the Lyapunov equation (14). The curve from figure 8 is replotted in figure 9 and is now labeled "full-state feedback cases." This curve serves as a lower bound to all the other cases, where a Kalman filter is used in the feedback loop. Three curves are shown, each for a different ratio of disturbance to measurement noise. These curves are also lines of constant Kalman filter gain. In all cases the normalized disturbance level is kept at 10 percent. The parameter for these curves is  $\tilde{\psi}_W/\tilde{\psi}_V$ , the ratio of normalized disturbance to measurement noise. As  $\tilde{\psi}_W/\tilde{\psi}_V$  increases (less measurement noise), the curves approach the

full-state feedback curve. The dashed lines indicate loci of constant control gains; each locus is labeled with the control weighting  $r_2$  used for the control design. For any fixed set of control gains, performance is sacrificed when a Kalman filter is introduced into the loop:  $\tilde{\sigma}_{P_7}$  increases along a constant-control-gain locus as  $\tilde{\psi}_w/\tilde{\psi}_v$  increases.

One important difference between full-state and Kalman filter feedback can be noted by comparing the respective curves as  $\tilde{\sigma}_{Q_a}$  gets large. For full-state feedback,  $\tilde{\sigma}_{P_7}$  gets very small; but for Kalman filter feedback, the curves asymptotically approach constant values of  $\tilde{\sigma}_{P_7}$ . The reason is that the best a control with a Kalman filter in the loop can do is to drive the estimate of  $P_7$  to zero. The irreducible error remaining is simply the error incurred in estimating  $P_7$ . Shown in figure 9 are the asymptotic values of  $\tilde{\sigma}_{P_7}$  for the three Kalman-filter-gain curves and one corresponding to a  $\tilde{\psi}_w/\tilde{\psi}_v$  of 1950 (curve not shown). These asymptotic values, which are elements of the error covariance matrix  $P$ , are obtained automatically when solving the Kalman-filter Riccati equation.

Figure 9 thus summarizes the rms performance of a large number of pogo controller designs; each employs  $P_7$  measurement and a Kalman filter in the feedback loop. Kalman filter feedback is more complicated than full-state feedback because the measurement noise level must be determined. For example, suppose that the maximum allowable value of  $\tilde{\sigma}_{Q_a}$  is 4.5 percent, the value used in the previous section on full-state feedback design. Suppose also that sensor noise is such that  $\tilde{\psi}_w/\tilde{\psi}_v$  is 19.5. And assume that the sensor noise is colored in the same way that the  $\tilde{Q}_{d7}$  disturbance is colored. Then the rms value of sensor noise can be computed as 0.52 percent. Figure 9 shows that, for this design, normalized rms HPOP suction pressure would be about 3 percent, rather than the 1.7 percent for full-state feedback. For this case, the closed-loop signal-to-noise ratio on the  $P_7$  sensor was 17 percent.

Although acceptable performance can be achieved with Kalman filter feedback, the problem of complexity remains. As formulated, any of the Kalman designs requires a 43rd-order system to be implemented. To determine whether simplifications are possible, we are led to view the Kalman filter - feedback gain combination as a single-input, single-output compensator.

### Frequency-Domain Interpretation of Kalman Filter Feedback

It is instructive to view the combination of a Kalman filter plus state-estimate feedback as a frequency-domain compensator (controller). The primary motive is to

see whether significant simplifications can be made in the controller. The following equations describe the controller:

$$\dot{\hat{x}} = A\hat{x} + Bu + K_e(y - H\hat{x}) \quad (18)$$

$$u = -K_c\hat{x} \quad (19)$$

where equation (18) is the Kalman filter equation (eq. (11)), repeated here for convenience, and equation (19) defines state-estimate feedback. Taking the Laplace transform of equation (18) for zero initial conditions and combining with equation (19) results in the transfer function matrix of the controller

$$u(s) = -K_c [sI - (A - BK_c - K_e H)]^{-1} K_e y(s) \quad (20)$$

The overall system, configured to show the feedback compensator, is shown in figure 10. Here,  $u(s) = u_a(s)$  and  $y(s) = P_{7m}(s)$  are scalars. Hence equation (20) can be expressed as

$$u_a(s) = G_c(s)P_{7m}(s) \quad (21)$$

to define the controller transfer function  $G_c(s)$ .

The main variable parameters that define the characteristics of  $G_c(s)$  are the control gain  $K_c$  and the Kalman filter gains  $K_e$ . These gains in turn are functions of  $r_2$  and  $\tilde{\psi}_w/\tilde{\psi}_v$ , respectively. To examine the structure of  $G_c(s)$ , various controller transfer functions were calculated for various pairs of  $r_2$  and  $\tilde{\psi}_w/\tilde{\psi}_v$ . Figure 11 compares three feedback-compensator transfer functions in terms of normalized frequency-response magnitude and phase. Commanded flow rate  $u_a(s)$  and measured HPOP pressure  $P_{7m}(s)$  were normalized as was done previously. The comparison is presented for controllers having the same set of Kalman filter gains ( $\tilde{\psi}_w/\tilde{\psi}_v = 1.95$ ) but for three control weightings  $r_2$ . All controllers are stable, as was determined by calculating the eigenvalues of  $A - BK_c - K_e H$ . This is a convenient result but is not always the case with such Kalman filter - LQR-designed controllers. This fact was pointed out by Kwatny and Fink (ref. 6), who designed controllers based on a Kalman filter and found that the overall closed-loop system response was stable but that in some cases the controller by itself was unstable.

The magnitude plot of figure 11(a) shows major peaks in the controller response near 2.3 and 23.8 hertz. This would be expected since this is where the least-stable system modes occur. The main trend shown is that, as control weighting  $r_2$  was decreased, controller gain increased - at all frequencies. Although not shown, similar

results were obtained when the  $\tilde{\psi}_w/\tilde{\psi}_v$  ratio was varied. In particular, when  $\tilde{\psi}_w/\tilde{\psi}_v$  was increased, controller gain increased.

The phase angle plot (fig. 11(b)) shows that the controllers all exhibit large amounts of phase lag. However, for smaller values of  $r_2$  (higher gain controllers), phase lag is less. Controller poles and zeroes were calculated to determine why the controllers have such large amounts of phase lag. Each of the three controllers in figure 11 had right-half-plane zeros in its transfer function, which caused the additional phase lag. Using a controller with right-half-plane zeroes is contrary to common practice with classical frequency-domain techniques. However, Shaw (ref. 7) gives a root-locus example wherein right-half-plane zeroes are required to achieve a desired set of closed-loop poles. Thus, the existence of right-half-plane zeroes in the present results is unexpected but plausible. In particular, controllers designed for  $r_2$  of  $2 \times 10^{-3}$  and  $2 \times 10^{-4}$  both have 41 zeroes, 17 of which are in the right half-plane. The controller for an  $r_2$  of  $2 \times 10^{-5}$  has 41 zeroes, 13 in the right half-plane. The phase angles for these cases differ because the four additional right-half-plane zeroes for  $r_2$  of  $2 \times 10^{-3}$  and  $2 \times 10^{-4}$  occur near 24 and 40 hertz, causing additional  $180^\circ$  phase lags there (fig. 11(b)).

### Non-Minimum-Phase Controllers

For a better understanding of the presence of right-half-plane zeroes, transfer function zeroes were calculated for various controller designs. Results for selected designs are given in table III, which lists the number of right-half-plane controller zeroes for various combinations of  $r_2$  and  $\tilde{\psi}_w/\tilde{\psi}_v$ . The conclusion that is suggested by the table is that, in general, the higher the controller gain, the fewer the number of right-half-plane zeroes. Higher gain means either higher optimal control gains or higher filter gains. Further down the table and to the right, the number of right-half-plane zeroes decreases. In fact, the highest gain controller ( $\psi_w/\psi_v = 195$ ,  $r_2 = 4 \times 10^{-6}$ ) has no right-half-plane zeroes at all. From these results, we concluded that a low-control-effort stabilizing pogo controller will tend to have right-half-plane zeroes. This somewhat counterintuitive conclusion was also reached by Widnall (ref. 8) in a sampled-data optimal control design of the Apollo autopilot. There are similarities between his problem and the pogo stabilization problem in that both systems to be controlled are unstable and contain a number of lightly damped modes. Thus low-control-effort optimal control of unstable plants appears to lead to non-minimum-phase controllers.

The remaining problem was to simplify the controller designs to a transfer function of reasonable order (10th to 15th order). A method developed by Hutton and

Friedland (ref. 9) was used on a representative transfer function for an  $r_2$  of  $2 \times 10^{-3}$  and a  $\tilde{\psi}_w/\tilde{\psi}_v$  of 1.95. The technique produces a series of reduced-order transfer function approximations, beginning with 43rd order and extending down to any arbitrary lower order approximation. For reduced transfer function orders of less than about 30 the transfer function fits were poor, probably because the non-minimum-phase character of the transfer function made simplifying difficult. Thus, we decided not to pursue the Kalman filter approach further but instead to look into simplifying the full-state feedback designs by eliminating certain of the feedback variables.

### Partial-State-Feedback Minimum-rms Control Designs

Sophisticated output-feedback techniques for simplifying LQR designs were discarded in favor of a much simpler, intuitive approach. Gain simplification was performed as follows: The feedback variables consist of four types - flow rates, pressures, structural velocities, and structural displacements. Thus, gains were grouped into four classes, and plots were made of each class for various LQR designs. In all plots, gain values were normalized. Velocity gains were normalized by the acoustic velocity in liquid oxygen (51 800 cm/sec; 20 400 in/sec), and displacement gains were normalized by the line lump length (345 cm; 136 in.). Gain (absolute) magnitudes were compared within each group. Then only the gains with the largest magnitudes were retained for use in the simplified gain control. It is difficult to rationally compare gains from one class with those from another. As discussed later in this section, other rationale were used to eliminate complete classes of gains.

Figure 12 summarizes the results. Figure 12(a) shows the flow-rate gains as a function of the inverse of the control weighting parameter  $r_2$ . Here, gains for states 25 (LPOP exit flow rate), 27 (thrust chamber flow rate), and 29 (suppressor output flow rate) are obviously predominant. Thus, we decided to discard the rest of the flow-rate gains and keep these three. Figure 12(b) shows normalized pressure gains as a function of  $r_2^{-1}$ . Most gains increase with decreasing  $r_2$ , but the most notable result is that gains for states 24 (LPOP suction pressure) and 26 (HPOP suction pressure) are dominant. This result is not unexpected because HPOP suction pressure was weighted in the performance index. Figure 12(c) shows the gains for the generalized displacements. The dominant gains correspond to the displacements of the last two modes. From figure 12(d), it is not apparent that any of the normalized, generalized velocity gains are dominant. For this reason and so that measuring (or reconstructing) all the structural velocity states could be avoided, we decided to eliminate all structural variables from the feedback loops. There remain two gains unaccounted for: those associated with the noise-coloring states. These states are unmeasurable

and to include them would have meant implementing an observer to reconstruct them; thus they too were dropped.

The gains left then were those for LPOP inlet flow and pressure, HPOP inlet pressure and outlet flow, and suppressor outlet flow. The performances of these simplified-gain, minimum-rms control designs are compared with those of the full-state feedback designs in figure 13. The rms performances of four simplified gain designs are compared with the performances of the full-state feedback designs upon which they were based. The base  $r_2$  values chosen were  $2 \times 10^{-3}$ ,  $2 \times 10^{-4}$ ,  $2 \times 10^{-5}$ , and  $2 \times 10^{-6}$ . All simplified gain designs were stable, a fact not guaranteed by the gain elimination process. For any fixed value of  $\tilde{\sigma}_{Q_a}$ , the simplified gain control is inferior to the corresponding full-state feedback control. Controls compare least favorably at the higher values of rms suppressor flow. However, for the lower values, for instance for a  $\tilde{\sigma}_{Q_a}$  of 4, the simplified design is not much worse than the full-state feedback design. It is in this region of  $\tilde{\sigma}_{Q_a}$  that the practical upper limit on  $\tilde{\sigma}_{Q_a}$  would probably lie. Thus, it appears that simplified gain designs are a reasonable solution to the suppressor design problem as long as the lower values of  $\tilde{\sigma}_{Q_a}$  are used.

As a check on the results shown in figure 13, a closed-loop frequency response was run for the lowest-gain simplified gain control shown in figure 13 (based on the full-state feedback control designed for an  $r_2$  of  $2 \times 10^{-3}$ ), whose normalized rms suppressor flow requirement is about 4. Figure 14 compares this response to the open-loop frequency response. Closed-loop performance is quite acceptable because the disturbance is everywhere attenuated to values below open loop, as was the case for full-state feedback. Comparing figures 14 and 7(a) shows that, except for the region near 25 hertz, the simplified feedback design is very close in performance to the full-state feedback design, and both designs use essentially the same amount of suppressor flow.

A major concern with any control system, optimal or otherwise, is how sensitive the closed-loop response is to changes in system parameters that may be imprecisely known. Therefore, we decided to check the sensitivity of the closed-loop response of the simplified gain design shown in figure 14 to changes in key system parameters. Experience has shown that two parameters that have major effects on system stability are the frequencies of the first and sixth structural modes. Thus, the frequencies of these modes were varied, and the frequency responses were calculated for the system that uses the simplified gain controller. Figure 15 shows a check case where the frequency of the sixth structural mode (23.8 Hz) was increased by 10 percent. There was no serious performance degradation. Similar results were observed when the first structural modal frequency was varied.

In summary then, it has been demonstrated that a partial-state feedback control for pogo suppression can be designed. The gain elimination procedure used was effective in eliminating less important feedback variables. For higher performance controls, those that require large amounts of control effort, the simplified controls suffered appreciable performance degradation. However, for lower performance controls, simplified gain control was nearly as good as full-state feedback. Sensitivity of the simplified controls does not appear to be a significant problem.

## MODAL CONTROL APPROACH TO SUPPRESSOR CONTROL DESIGN

The second approach taken in designing a control to suppress pogo oscillations is designated the "modal control design" approach. As already mentioned, the aim in the modal control approach is to increase the damping on the least stable or most sensitive system modes while not unreasonably increasing the modal frequencies associated with the actuator. The focus in this design method is primarily on the degree of stability, with secondary focus on minimizing system response to disturbances.

The LQR and Kalman filter techniques lend themselves directly to this approach. The key difference between the modal control approach and the minimum-rms approach is in the selection of the quadratic performance index to be minimized. The difference in the character of the index then leads to differences in the resulting control systems.

### Performance Index Formulation

The first step in the modal control approach is to obtain the modal form of the system state-variable model. For the system state-variable equation

$$\dot{x} = Ax + Bu \quad (22)$$

a modal state vector  $\eta$  can be defined as

$$\eta = T^{-1}x \quad (23)$$

where the matrix  $T^{-1}$  effects the transformation from the original system coordinates into modal coordinates. The modal state equations can be obtained by substituting for  $x$  in equation (22) from equation (23):

$$\dot{\eta} = \Lambda\eta + T^{-1}Bu \quad (24)$$

where  $\Lambda = T^{-1}AT$ .

One convenient form of modal state equation can be obtained if the matrix  $\Lambda$  is the block-diagonal form of  $A$ , whose structure is

$$\Lambda = \begin{bmatrix} \Lambda_1 & & & 0 \\ & \Lambda_2 & & \\ & & \ddots & \\ 0 & & & \Lambda_k \end{bmatrix} \quad (25)$$

An element  $\Lambda_i$  is either (1) a scalar equal to a real eigenvalue  $\alpha_i$  of  $A$  or (2) a two-by-two matrix of the form

$$\Lambda_i = \begin{bmatrix} \alpha_i & -\beta_i \\ \beta_i & \alpha_i \end{bmatrix} \quad (26)$$

where  $\alpha_i$  and  $\beta_i$  are real and imaginary parts of a complex eigenvalue pair of  $A$ . With  $\Lambda$  being block diagonal, the matrix  $T$  becomes the modified eigenvector matrix (ref. 5). The block-diagonal, modified eigenvector matrix form of the eigenvalue-eigenvector problem is used here for computational convenience because no complex arithmetic is required.

The quadratic performance index that allows the designer to obtain a control that tends to increase the damping on certain selected system modes is set up as follows: First, the eigenvalues of the matrix  $A$  are obtained. From the eigenvalues, a block-diagonal matrix  $\Lambda$  is formed. Next, the mode whose damping is to be increased is selected. There are then two modal states  $\eta_\ell$  and  $\eta_{\ell+1}$ , corresponding to this mode, that are to be altered. Penalizing these states in the performance index will cause their amplitudes to be attenuated. As it turns out (especially for lightly damped modes) an attenuation in  $\eta_\ell$  and  $\eta_{\ell+1}$  will lead to an increase in damping of the associated mode. Thus, the "modal" performance index  $J_M$  can be written as

$$J_M = \int_0^\infty \left[ \gamma_\ell (\eta_\ell^2 + \eta_{\ell+1}^2) + u^T R_2 u \right] dt \quad (27)$$

where the integral form is used for  $J_M$  since random disturbances are not considered explicitly in the modal approach. Now the remaining step is to express  $\eta_\ell$  and  $\eta_{\ell+1}$

in terms of the original state vector  $x$ . It is assumed that matrix  $T^{-1}$  has been calculated. Define

$$T^{-1} = \begin{bmatrix} \hat{t}_1 \\ \hat{t}_2 \\ \cdot \\ \cdot \\ \cdot \\ \hat{t}_\ell \\ \hat{t}_{\ell+1} \\ \cdot \\ \cdot \\ \cdot \\ \hat{t}_n \end{bmatrix} \quad (28)$$

where  $\hat{t}_i$  are row vectors. Then  $\eta_\ell = \hat{t}_\ell x$  and  $\eta_{\ell+1} = \hat{t}_{\ell+1} x$ , from equation (23). Now if  $\eta_\ell$  and  $\eta_{\ell+1}$  are substituted into equation (27), the standard form

$$J_M = \int_0^\infty (x^T R_1 x + u^T R_2 u) dt \quad (29)$$

is obtained for  $J_M$ , where the elements of  $R_1$  are

$$(r_1)_{i,j} = \gamma_\ell (\hat{t}_{\ell i} \hat{t}_{\ell j} + \hat{t}_{\ell+1, i} \hat{t}_{\ell+1, j}) \quad (30)$$

To control the damping on other modes in addition to these, simply identify the indices of the associated modal states ( $m, m+1, p, p+1$ , etc.) so that the elements of  $R_1$  become

$$(r_1)_{i,j} = \sum_{k=\ell, m, p, \dots} \gamma_k (\hat{t}_{ki} \hat{t}_{kj} + \hat{t}_{k+1, i} \hat{t}_{k+1, j}) \quad (31)$$

where  $k$  takes on the values of the first indices of penalized modal state pairs.

## Full-State Feedback

As already discussed, the two least stable modes of primary interest in the liquid-oxygen-system model were those at 2.3 and 23.8 hertz. These modes are referred to as "critical modes" (fig. 3). Other modes, which although lightly damped were not considered, were those at 4.72, 22.5, and 8.38 hertz. These modes are very insensitive to control and system parameter variations and never become unstable. Thus, all effort was concentrated on increasing damping on the 2.3- and 23.8-hertz modes. Full-state feedback designs were calculated for the case where both critical modes were equally weighted. The primary criterion for judging effectiveness is the increase in modal damping on these two modes.

Table IV shows the results obtained for two different control weightings  $r_2$ . For a weighting of 0.1, damping on both modes was in excess of 10 percent, which is generally considered an acceptable target design value. All other modes were essentially unchanged. For both cases, the 50-hertz actuator pole was not moved appreciably. This shows that the two modal designs quite efficiently concentrate available control energy on only the two selected modes (2.3 and 23.8 Hz).

Eigenvectors associated with these designs were plotted so that insight could be gained into the behavior of the modal designs. The propulsion system portions of the eigenvectors (corresponding to the states that are either pressures or flow rates) were plotted as either pressure mode (figs. 16(a) and (b)) or flow mode (figs. 16(c) and (d)) shapes. The mode shapes are simply the normalized magnitudes of the (pressure or flow rate) eigenvector components plotted as a function of the spatial location of the corresponding pressure or flow-rate variable. Figures 16(a) and (b) present the pressure mode shapes for both the 23.8- and 2.3-hertz modes. One open-loop and two closed-loop, full-state feedback cases are shown. A propulsion system schematic is included along the abscissa to aid in locating the spatial coordinates of the various pressures throughout the system. Five maximums occur for the 23.8-hertz mode shape (fig. 16(a)); all have about the same magnitude in the open-loop case. For full-state feedback, as control weighting is decreased, the pressure maximums along the feedlines decrease relative to the highest maximum, which now occurs at the HPOP inlet location. Because each case is normalized with respect to its highest maximum, no comparisons can be made between cases. But we can conclude that the control changes the way in which pressure perturbations affect the pressure distribution within the system. An increase in the amount of control decreases the effect of a perturbation on HPOP inlet pressure, as discussed in the section Frequency-Domain Behavior of Modal Control Designs.

The 2.3-hertz mode shape (fig. 16(b)) was less sensitive to control than was the 23.8-hertz mode. However, the modal damping ratio for an  $r_2$  of 0.1 was almost

1000 times greater than the open-loop ratio.

The flow mode shapes in figures 16(c) and (d) are like those in figures 16(a) and (b). Generally, flow is  $90^\circ$  out of phase with pressure, as would be expected. Again, increased control tends to alter the mode shape away from the open-loop, organ-pipe-like pattern. No clear pattern exists for the modal amplitude of control flow (state 29) as control weighting is decreased. This is true for both the 23.8- and 2.3-hertz modes.

### Sensitivity of Full-State Feedback Designs

The modal design approach has been shown to be a very selective method. In it, the control is required to modify the system frequency response only in regions about the (two) selected modes. Because of this selectivity, the resulting designs could be overly sensitive to parametric variations and large increases in modal damping might not be achieved if system parameters changed. Thus, eigenvalue calculations were performed for off-nominal cases, where the most critical system parameters were varied.

For the pogo model of this study, there are a number of parameters whose values are imprecisely known. But the most critical ones, it is generally believed, are the structural modal frequencies. Thus, off-nominal runs were made in which the 2.3- and 23.8-hertz modal frequencies were varied to see how they influenced the closed-loop modal damping ratios. Gains for the lower gain modal design (for  $r_2 = 1.0$ ) were used throughout. Figures 17(a) and (b) show how the damping ratios for all modes less than 30 hertz varied as structural modal frequencies were varied  $\pm 10$  percent from nominal. Modes greater than 30 hertz were influenced very minimally. In figure 17(a), the 2.3-hertz mode was varied. The only closed-loop mode whose damping ratio varied appreciably was the (nominally) 2.89-hertz mode. However, its damping is well above 16 percent over the range of variation.

In figure 17(b) the 23.8-hertz modal frequency was varied  $\pm 10$  percent. As a result a number of damping ratios changed, the most troublesome being the 26.3-hertz mode. However, its lowest damping ratio is about 1 percent, which is still an acceptable value. The 23.8-hertz modal frequency appears to be a much more influential parameter than the 2.3-hertz mode. Thus, for any final design, it would be advisable to more thoroughly investigate the sensitivity of any designs to the 23.8-hertz modal frequency.

## Partial-State Feedback

Although the results and modal designs just discussed are useful as baseline information, such designs would be impractical to implement in full-state feedback form. Implementing a Kalman filter would be one solution to the problem. But, because of the rather selective nature of the performance index, we believe an adequate job could be done more simply by using partial-state feedback. To see what gains might be eliminated, control gains for designs with  $r_2$  of 1 and 0.1 were tabulated (table V). In scanning the table, it is obvious that the largest gains occur for states 30, 31, 40, and 41. This is not surprising, as these states are associated with the 2.3- and 23.8-hertz modes; that is, they are the modal displacements and velocities for both modes. These two modes were the only ones weighted in the modal performance index. Thus, the partial-state feedback designs considered for further analysis used only states 30, 31, 40, and 41.

### Generation of Unmeasurable Modal State Variables

Partial-state feedback involving only states 30, 31, 40, and 41 still cannot be implemented because these states are generalized structural displacements and velocities and are thus not directly measurable. The way to get around this problem is to look at the equation relating structural outputs (which are physical quantities and can be measured) to the structural states. This equation is given in appendix B and is repeated here for convenience.

$$y_s = C_s x_s + \bar{C}_s \dot{x}_s \quad (32)$$

Matrix  $\bar{C}_s$  accounts for the liquid-oxygen-tank outflow effects. Its only nonzero elements are  $\mathcal{P}_i(\text{tb})$ ,  $i = 1, \dots, 6$ , for the six-structural-mode model. However, for the model considered, all  $\mathcal{P}_i(\text{tb})$  are zero except for  $\mathcal{P}_1(\text{tb})$ , which is  $-2.16 \times 10^{-3}$ . System frequency responses and eigenvalues were calculated by assuming that  $\mathcal{P}_1(\text{tb})$  is zero, that is, by neglecting all tank outflow effects. Very little difference was noted with and without  $\mathcal{P}_1(\text{tb})$ ; therefore it was assumed that

$$y_s \cong C_s x \quad (33)$$

Now, from the  $C_s$  matrix (table VI), it is evident that not all structural outputs are independent. In fact, only six independent structural outputs can be defined. This six-element output vector, denoted as  $\tilde{y}_s$ , can be defined as

$$\tilde{y}_s \triangleq \begin{pmatrix} \dot{x}_{l1} \\ \dot{x}_1 = \dot{x}_3 \\ \dot{x}_4 = \dot{x}_7 \\ \dot{x}_{tb} \\ \dot{z}_{l2} = \dot{z}_1 = \dot{z}_3 \\ \dot{z}_4 = \dot{z}_7 \end{pmatrix} \quad (34)$$

By using  $C_s$  as defined in appendix B and the modal data given in table II, the output vector  $\tilde{y}_s$  can be related to the six generalized structural velocities as follows:

$$\begin{pmatrix} \dot{x}_{l1} \\ \dot{x}_1 \\ \dot{x}_4 \\ \dot{x}_{tb} \\ \dot{z}_{l2} \\ \dot{z}_4 \end{pmatrix} \cong \begin{bmatrix} -1.267 & -0.198 & 0.054 & 0.022 & 0.022 & 0.022 \\ -0.8 & -0.245 & -0.0787 & -0.752 & 0.370 & 0.0134 \\ -2.38 & 0.239 & -0.556 & -1.71 & -2.13 & 2.63 \\ -0.137 & -0.334 & -0.259 & -7.74 & 4.44 & 5.34 \\ -0.316 & -0.352 & 0.431 & -0.372 & 0.017 & -0.09 \\ -2.68 & 0.50 & -1.95 & -0.12 & 0.99 & -1.56 \end{bmatrix} \begin{pmatrix} \dot{q}_1 \\ \dot{q}_2 \\ \dot{q}_3 \\ \dot{q}_4 \\ \dot{q}_5 \\ \dot{q}_6 \end{pmatrix} \quad (35)$$

or, more compactly,

$$\tilde{y}_s \cong C_\alpha x_\alpha \quad (36)$$

where

$$x_\alpha^T = (\dot{q}_1, \dot{q}_2, \dot{q}_3, \dot{q}_4, \dot{q}_5, \dot{q}_6) \quad (36)$$

Next, so that velocities  $x_\alpha$  can be reconstructed,  $C_\alpha$  must have an inverse, which it does. In fact, it was calculated to be

$$C_\alpha^{-1} \triangleq \hat{C}_\alpha = \begin{bmatrix} -0.7248 & 1.852 & -0.06638 & -0.09701 & -1.347 & -0.3606 \\ 0.09167 & -13.70 & 0.3960 & 0.7353 & 9.771 & 2.505 \\ 1.6650 & -7.951 & 0.1027 & 0.4207 & 6.506 & 1.179 \\ 1.119 & 1.707 & -0.2015 & -0.1130 & -2.621 & -0.5447 \\ 0.8755 & -0.6522 & -0.2674 & 0.1380 & -0.2871 & 0.04502 \\ 0.9128 & 1.821 & -0.04165 & -0.02731 & -2.668 & -0.6223 \end{bmatrix} \quad (37)$$

Thus,

$$\mathbf{x}_\alpha = \hat{\mathbf{C}}_\alpha \tilde{\mathbf{y}}_s \quad (38)$$

Finally, the two generalized velocities ( $\dot{\mathbf{x}}_{31} = \dot{\mathbf{q}}_1$  and  $\dot{\mathbf{x}}_{41} = \dot{\mathbf{q}}_6$ ), which need to be reconstructed, can be obtained as

$$\left. \begin{aligned} \dot{\mathbf{q}}_1 &= \sum_{i=1}^6 \hat{\mathbf{C}}_{\alpha 1, i} \tilde{\mathbf{y}}_{si} \\ \dot{\mathbf{q}}_6 &= \sum_{i=1}^6 \hat{\mathbf{C}}_{\alpha 6, i} \tilde{\mathbf{y}}_{si} \end{aligned} \right\} \quad (39)$$

Therefore to generate or reconstruct each generalized velocity requires the sensing of six structural velocities and the weighted summing of these velocities where the appropriate row elements of matrix  $\hat{\mathbf{C}}_\alpha$  are the weights. The two generalized displacements can be generated by integrating the respective generalized velocities. In an actual application, the only available structural measurements would be from accelerometers. These accelerometer outputs would need to be high-pass filtered to remove any low-frequency component, linearly combined according to equation (39), and then bandpass filtered at the associated modal frequencies to determine the reconstructed modal velocities. This process would eliminate concern over the effect of any modes present but not considered in the pogo model, except for those that might occur in a filter passband. If an extraneous mode does occur in a passband, additional information would be required to separate out its effects.

Other methods of generating the generalized velocities from the direct use of parallel bandpass-filtered data from one or more structural accelerometers can be conceived of. The important aspect is that the information required about the generalized modes that can destabilize through pogo coupling be supplied to the controller. Then with this information, the control energy can be concentrated at the offending modal frequency.

At this point, the partial-feedback modal designs could have been further simplified. However, because it was not obvious which elements of the  $\mathbf{C}_\alpha$  matrix could be dropped, this aspect was not pursued. In the following sections, modal designs are further evaluated on the basis of eigenvalue-damping-sensitivity mode shapes and are finally compared with minimum-rms designs.

## Mode-Shape Analysis of Partial-State Feedback Design

The partial-state feedback design that was evaluated used reconstructed estimates of states 30, 31, 40, and 41 ( $q_1$ ,  $\dot{q}_1$ ,  $q_6$ , and  $\dot{q}_6$ ). The full-state feedback modal design obtained for a control weighting  $r_2$  of 1 was used as the basis from which the modal partial-state feedback design was obtained.

In the partial-state design, damping may be decreased because fewer states are fed back than in the full-state design. For instance, the damping on the 23.8-hertz mode decreased from 3.67 percent to 2.42 percent in going to partial-state feedback. However, damping on the 2.3-hertz mode increased slightly, from 4.49 percent to 4.87 percent. At any rate, it can be concluded here that for the four states chosen for feedback, the dampings on the two modes of primary interest remain well above the allowed minimum of 1 percent.

Flow and pressure mode shape plots like those in figure 16 are presented in figure 18 to clarify what happens when a full-state feedback design is simplified. Here, full- and partial-state feedback mode shapes are compared for the 23.8- and 2.3-hertz modes. First, the 2.3-hertz mode shapes for both flow and pressure are almost identical for full- and partial-state feedback. From this and the eigenvalue damping numbers, it can be concluded that little performance was lost in eliminating most of the gains insofar as the 2.3-hertz mode is concerned.

Differences in shapes do occur, however, for the 23.8-hertz mode. In figures 18(a) and (b), for instance, the partial-state feedback mode shape looks like one for a lower gain design; that is, it is more like an open-loop shape. This agrees with the fact that the damping ratio is less for the partial-state case (again, more like an open-loop ratio). The flow mode shapes for the 23.8-hertz mode show the most pronounced differences. Mode shapes in the vertical and horizontal feedlines are similar, with partial-state feedback giving a mode shape more like open loop. The main differences occur in the interpump duct for interpump duct flow  $Q_5$  and suppressor flow  $Q_a$ . The interpump duct flows have a lower modal amplitude with partial-state feedback, and again this control looks more like an open-loop control in this region. This fact can be observed by comparing the open-loop mode shape values for  $Q_5$  from figures 16(c) and (d) with the value shown in figure 18.

## Sensitivity of Partial-State Feedback Designs

One of the drawbacks to partial-state feedback is increased sensitivity to parametric variations. This is obvious if the modal damping sensitivity in figure 19(a) is compared with that of the full-state feedback case (fig. 17(a)) upon which the partial-state design is based. At nominal conditions, some damping ratios are less for the partial-

state feedback case, notably for the 2.89- and 23.3-hertz modes. But these modes are quite heavily damped and the rest of the damping ratios are almost identical for full- and partial-state feedback. The main deficiency in the partial-state case is that there is an appreciable decrease in damping of the 2.3-hertz mode (off nominal). For full-state feedback, this modal damping is insensitive. However, at its worst, the damping ratio is still an acceptable 1.5 percent.

The sensitivity of partial-state feedback to changes in the 23.8-hertz mode is shown in figure 19(b). Comparing it with figure 17(b) shows that except for the 8.6-, 23.3-, and 2.89-hertz modes, damping ratios and sensitivities are approximately the same with the full- and partial-state feedback. Fortunately, the damping ratios for these three modes are all above 2 percent in the  $\pm 10$ -percent range of parametric variation. Thus, partial-state feedback affords quite adequate closed-loop stability.

#### Comparison of Modal Control and Minimum-rms Designs

The main thrust of the modal control design approach has been, naturally, to judge all designs according to the positions of their eigenvalues without regard to input and output behavior. This contrasts with the minimum-rms approach where input and output behavior is of main concern. Both approaches are valid; but it is instructive to examine modal control designs in terms of their rms behavior. This was done for the full- and partial-state feedback modal designs: The rms response values were calculated by using the same colored-noise disturbance that was used to evaluate minimum-rms designs. The results are shown in figure 20, where normalized rms values of  $P_7$  are plotted as a function of normalized suppressor flow rate. For comparison, the minimum-rms, full-state feedback designs are shown by the solid line. The modal full- and partial-state design results are shown as the circles and squares, respectively.

A number of points can be noted in figure 20. First, the modal designs used relatively small amounts of suppressor flow. This correlates with the fact that actuator poles for these designs are moved very little from the open-loop locations. Second, these modal designs can be characterized as low-gain, stabilizing controls. Third, the rms performances of full- and partial-state modal designs are not radically different, especially for the lower gain designs. However, none of the modal designs are close in rms performance to the minimum-rms, full-state feedback designs. This is to be expected since the design criteria for modal control designs differ from those for minimum-rms designs.

## Frequency-Domain Behavior of Modal Control Designs

For further insight into the modal control designs, a frequency-domain analysis was made. Thus, modal designs can be compared with previously discussed minimum-rms designs based on transfer function representations. Figure 21 shows open- and closed-loop frequency responses (magnitude only) for a modal design with full-state feedback. The main result is that disturbance  $\tilde{Q}_{d7}$  is suppressed only in frequency bands near the two critical modal frequencies. Contrasting this to the minimum-rms response shown in figure 7(a), where disturbance suppression occurs throughout the range of frequencies shown, again emphasizes the selectivity that is achieved with the modal design. This frequency selectivity is also apparent in figure 22, where the closed-loop response of the control to disturbance is shown. Only two peaks occur in this plot - near 2.3 and 23.8 hertz, a result that is in sharp contrast to the many-peaked curve in figure 7(b) for a minimum-rms design.

Going from full- to partial-state feedback causes little change in the frequency response of  $\tilde{P}_7$  to disturbance  $\tilde{Q}_{d7}$ . The response for partial-state feedback (fig. 23) is similar to the response of the original full-state feedback design (fig. 21), a fact that suggests the rms performances would also be similar. This, too, is the case, as shown in figure 20, where the leftmost circle and square are the points for the cases in question. Figure 20 also shows that normalized suppressor flow is less for the partial-state feedback simplification than for full-state feedback. (Compare figs. 22 and 24 and the areas under the frequency responses for commanded suppressor flow rate.) The plot for the partial-state feedback case (fig. 24) encloses less area than does the plot for the full-state feedback case. In addition, a number of peaks occur in figure 24 that do not occur in figure 22. Thus, for partial-state feedback, the control attempts to attenuate disturbances at frequencies other than those near the two critical modes. This type of behavior was not expected based on the performance index used. However, such undesired control activity is not of significant magnitude to be a problem.

## Use of Kalman Filter with Modal Control Designs

As a final variation on designs that could be implemented based on the modal control concept, a Kalman-filter-based controller was investigated. For this study, it was assumed that only HPOP suction could be measured, as was done for the minimum-rms design evaluations. Modal control gains for an  $r_2$  of 1 were combined with Kalman filter gains for a  $\tilde{\psi}_W/\tilde{\psi}_V$  of 195 to form a feedback compensator such as that shown schematically in figure 10. The frequency response for this compensator is shown in figure 25.

One significant feature of this compensator's magnitude response (fig. 25(a)) is that only two major peaks exist. However, responses for minimum-rms designs (fig. 11(a)) have many peaks in addition to those near 2.3 and 23.8 hertz. The fact that the response had many peaks probably caused difficulties when low-order transfer function fits were attempted. Because of the relatively simpler shape of the modal-control compensator's frequency response, low-order fits should be more feasible. The compensator's phase angle (fig. 25(b)) shows much less overall phase lag than do any of the phase angles in figure 11(b). This fact also makes it easier to obtain satisfactory low-order transfer function fits.

A study to obtain such reduced-order models was not attempted here. These results do suggest, though, that a viable control design solution might be a single  $P_7$  measurement fed through a doubly resonant low-order compensator.

## CONCLUSIONS

The feasibility of applying linear quadratic regulator techniques and Kalman filtering to the design of an active-pogo-suppression control system was studied. Two linear quadratic, optimal control approaches were taken: One minimized the root-mean-square response of high-pressure-oxidizer-pump suction pressure to a random disturbance. The other increased the damping on two system oscillatory modes that were deemed most critical to pogo oscillation. Ideal, full-state feedback designs were computed and then used as baseline cases. Physical reasoning was used to find practical, partial-state feedback designs. A number of potentially implementable, simplified controls were found:

1. Partial-state feedback, minimum-rms designs: These designs require sensing of two flow rates and two pressures. They increase stability of most system modes and reduce the overall system response to disturbances. Also, sensor requirements are not severe except those for a liquid-oxygen flow sensor, which may be a problem. These control designs were less able to increase damping on the critical system modes than were the modal control designs.

2. Partial-state feedback, modal control designs: Each design requires that a sufficient number of structural accelerations be measured and appropriately filtered in order to reconstruct desired modal state information. Implementation is thus somewhat more complex than for the designs described by Seidel in NASA TM X-3368. Control energy is concentrated in fairly narrow frequency bands, and large increases in damping are achieved for the two critical system modes. Parameter sensitivity is not a severe problem.

3. Reduced-order-feedback compensator based on modal control design using a

Kalman filter: This design uses only a single pressure measurement and a doubly resonant feedback compensator. The feasibility of obtaining a suitable low-order compensator looks promising.

In general, the linear quadratic regulator approach appears to be well suited to the design of active-pogo-suppression controllers. Further, it provides means by which the issue of control energy can be effectively dealt with.

Lewis Research Center,  
National Aeronautics and Space Administration,  
Cleveland, Ohio, July 18, 1978,  
505-05.

## APPENDIX A

### SYMBOLS

$A$	pogo system matrix, $43 \times 43$
$A_{cn}$	colored-noise matrix, $2 \times 2$
$A_p$	propulsion system matrix, $29 \times 29$
$\bar{A}_p$	partition of $A$ matrix, $29 \times 29$
$A_s$	structural system matrix, $12 \times 12$
$\bar{A}_s$	partition of $A$ matrix, $12 \times 12$
$A_1, A_2$	cross-sectional area, $cm^2$
$a$	acoustic velocity, m/sec
$B$	system input matrix, $43 \times 1$
$B_p$	propulsion system input matrix, $29 \times 1$
$\bar{B}_p$	partition of $A$ matrix, $29 \times 12$
$\bar{B}_s$	partition of $A$ matrix, $12 \times 29$
$C$	compliance, $cm^3/N$
$C_{b1}$	low-pressure-oxidizer-pump compliance, $cm^5/N$
$C_{b2}$	high-pressure-oxidizer-pump compliance, $cm^5/N$
$C_s$	structural output matrix, $12 \times 12$
$\bar{C}_s$	structural derivative output matrix, $12 \times 12$
$C_\alpha$	structural velocity matrix
$c_f$	discharge coefficient, dimensionless
$D$	disturbance matrix, $43 \times 1$
$D_{cn}$	colored-noise disturbance matrix, $2 \times 1$
$D_p$	propulsion system disturbance matrix, $29 \times 1$
$D_{ps}$	coupling matrix, $29 \times 12$
$D_{sp}$	coupling matrix, $6 \times 29$
$E_s$	structural mass matrix, $12 \times 6$

$F$	force, N
$F_q$	tank-pressure coefficient matrix, $6 \times 12$
$F_s$	generalized force matrix, $6 \times 12$
$\mathcal{F}$	generalized force, N
$\bar{f}$	mean mass flow of liquid oxygen, g/sec
$f_q$	element of $F$ matrix
$g$	gravitational constant, N/g
$H$	output matrix, $12 \times 43$
$H_{cn}$	noise-coloring output matrix, $1 \times 2$
$H_p$	partition of $H$ matrix, $12 \times 29$
$H_s$	partition of $H$ matrix, $12 \times 12$
$i$	component of vector
$J_M$	modal performance index
$J_R$	mean-square performance index
$j$	component of vector
$K_c$	control gain matrix
$K_e$	Kalman filter gain matrix
$L$	inertance, $N \cdot \text{sec}^2 / \text{cm}^5$
$l$	line length, cm
$M$	generalized mass, g
$m_1+1$	low-pressure-oxidizer-pump dynamic gain, dimensionless
$m_2+1$	high-pressure-oxidizer-pump dynamic gain, dimensionless
$P$	pressure, $N/\text{cm}^2$
$P_7$	high-pressure-oxidizer-pump suction pressure variation, $N/\text{cm}^2$
$P_{7m}$	measured value of $P_7$
$\mathcal{P}$	modal pressure coefficient, $N \cdot \text{sec}^2 / \text{cm}^3$
$p$	pressure in feedline lump, $N/\text{cm}^2$
$Q$	volumetric flow rate, $\text{cm}^3/\text{sec}$
$q$	generalized displacement, cm

$\bar{q}$	volumetric flow rate in feedline lump, $\text{cm}^3/\text{sec}$
R	resistance, $\text{N} \cdot \text{sec}/\text{cm}^5$
$R_1$	weighting matrix on states
$R_2$	weighting matrix on controls
$r_2$	element of R matrix (scalar)
T	modal transformation matrix
U	intermediate matrix, $6 \times 6$
u	control vector
$u_a$	commanded suppressor flow rate, $\text{cm}^3/\text{sec}$
V	intermediate matrix, $12 \times 12$
v	white-measurement noise vector
$W_1$	intermediate matrix, $12 \times 12$
$W_2$	intermediate matrix, $12 \times 29$
w	white-noise disturbance vector
$w_{cn}$	colored-noise disturbance vector
x	overall system state vector, $43 \times 1$
$x_{cn}$	colored-noise state vector, $2 \times 1$
$x_p$	propulsion system state vector, $29 \times 1$
$x_s$	structural system state vector, $12 \times 1$
$x_\alpha$	vector of generalized structural velocities, $6 \times 1$
y	output vector, $12 \times 1$
$y_s$	structural system output vector, $12 \times 1$
z	structural displacement along horizontal axis, cm
$\gamma$	weighting on modal state variable
$\zeta$	damping ratio
$\eta$	modal state vector
$\lambda$	block-diagonal matrix
$\rho$	liquid-oxygen density, $\text{g}/\text{cm}^3$
$\sigma(\ )$	rms value of ( )

$\tau_c$	time constant, sec
$\Phi$	mode shape vector, dimensionless
$\varphi$	modal displacement coefficient, dimensionless
$\psi_v$	power spectral density of v
$\psi_w$	power spectral density of w
$\omega$	structural pole natural frequency, rad/sec

**Subscripts:**

a	actuator
b1	bubble for low-pressure oxidizer pump
b2	bubble for high-pressure oxidizer pump
D7	disturbance at station 7
d	discharge line
I	inner pump duct
i	index
J	injector
j	index
k	index
L1	first (vertical) feedline
L2	second (horizontal) feedline
l	lump
n	structural mode
P1	low-pressure oxidizer pump
P2	high-pressure oxidizer pump
tb	tank base
tc	thrust chamber and discharge line

**Superscripts:**

x	x-direction
z	z-direction
~	normalized value
.	derivative with respect to time
(^)	element of inverse matrix

## APPENDIX B

### STATE-VARIABLE SPACE SHUTTLE POGO MODEL

This appendix describes the dynamic model of the space shuttle oxidizer (liquid oxygen) system used for this pogo controller design study. Although the model is basically the one described in references 2 and 4, it has been modified to meet the needs of this study as well as other studies (e.g., ref. 3) conducted at Lewis. The model can be divided into a structural portion and a propulsion system portion. The structural model, which is a six-mode approximation describing the liquid-oxygen-feedline motion, is based on one developed by the Aerospace Corp. and uses the structural mode shape data presented in references 2 and 4. The propulsion system portion, which was also developed by Aerospace Corp. but modified at Lewis, is a linear, lumped-parameter model of the liquid-oxygen feedlines, pumps, and thrust chamber dynamics. The two portions of the model are joined through drag and momentum force coupling terms.

#### System Geometry

For dynamic modeling purposes a simplified liquid-oxygen feedline-pump-chamber geometry, developed by the Aerospace Corp., was used (fig. 26). The system consists of the liquid-oxygen tank connected to a 31.1-meter- (102-ft-) long, 0.25-meter- (0.82-ft-) diameter vertical feedline; an elbow; and then an 8.47-meter- (27.8-ft-) long, 0.25-meter- (0.82-ft-) diameter horizontal feedline connected to the low-pressure oxidizer pump (LPOP). A short interpump duct connects the LPOP with the high-pressure oxidizer pump (HPOP), which pumps the liquid oxygen through a discharge duct into the thrust chamber. The suppressor is located at the inlet to the HPOP.

The Aerospace Corp. structural model defines seven liquid-oxygen-system structural elements that can move independently of one another: the tank, the two feedline segments, the two elbows, the LPOP, and the interpump duct - HPOP - discharge line - thrust chamber combination. As shown by the velocity coordinates in figure 26, the tank and the two feedlines can each move in only their axial directions ( $\dot{x}_{tb}$ ,  $\dot{x}_1$ , and  $\dot{z}_2$ ), but the elbows and pump assemblies are free to move both horizontally and vertically. Propulsion system dynamics are characterized by volumetric flow rates  $Q_i$  and pressures  $P_i$  throughout the system. The subscripts  $i$  correspond to station locations:  $tb$ , tank base; 1, first elbow; 2, entrance to horizontal feedline; 3, second elbow; 4, LPOP inlet; 5, LPOP exit; 7, HPOP inlet; and  $tc$ , thrust chamber. These station definitions are the same as those used in references 2 and 4.

## Propulsion System Dynamic Equations

The propulsion system portion is modeled as a lumped-parameter system. The vertical feedline is divided into nine lumps and the horizontal feedline into three lumps. Figure 27 shows a typical lump, or control volume, used in obtaining the feedline equations. Shown is the  $i^{\text{th}}$  lump, which occurs in the horizontal (second) feedline. The vertical feedline equations, which consider conservation of mass and momentum for each lump, can be written as

$$\begin{aligned} \dot{\bar{q}}_1 &= -\frac{R_\ell}{L_\ell} \bar{q}_1 - \frac{p_1}{L_\ell} + \frac{P_{tb}}{L_\ell} - \frac{R_\ell A_1}{L_\ell} \dot{x}_{\ell 1} \\ \dot{\bar{q}}_i &= -\frac{R_\ell}{L_\ell} \bar{q}_i - \frac{p_i}{L_\ell} + \frac{p_{i-1}}{L_\ell} - \frac{R_\ell A_1}{L_\ell} \dot{x}_{\ell 1} \quad i = 2, 3, \dots, 9 \\ \bar{q}_9 &\triangleq Q_1 \\ \dot{p}_i &= \frac{1}{C_\ell} (\bar{q}_i - \bar{q}_{i+1}) \quad i = 1, 2, \dots, 8 \\ p_8 &\triangleq P_1 \\ \dot{p}_9 &\triangleq \dot{P}_2 = \frac{1}{C_\ell} (Q_1 - Q_2 + A_1 \dot{x}_1 + A_1 \dot{z}_1) \end{aligned}$$

Similarly, the horizontal feedline equations can be written as

$$\begin{aligned} \dot{\bar{q}}_{10} &\triangleq \dot{Q}_2 = -\frac{R_\ell}{L_\ell} \bar{q}_{10} - \frac{p_{10}}{L_\ell} + \frac{P_2}{L_\ell} + \frac{R_\ell A_2}{L_\ell} \dot{z}_{\ell 2} \\ \dot{\bar{q}}_{11} &= -\frac{R_\ell}{L_\ell} \bar{q}_{11} - \frac{p_{11}}{L_\ell} + \frac{p_{10}}{L_\ell} + \frac{R_\ell A_2}{L_\ell} \dot{z}_{\ell 2} \\ \dot{\bar{q}}_{12} &\triangleq \dot{Q}_4 = -\frac{R_\ell}{L_\ell} \bar{q}_{12} - \frac{p_{12}}{L_\ell} + \frac{p_{11}}{L_\ell} + \frac{R_\ell A_2}{L_\ell} \dot{z}_{\ell 2} \end{aligned}$$

$$\dot{p}_{10} = \frac{1}{C_\ell} (\bar{q}_{10} - \bar{q}_{11})$$

$$\dot{p}_{11} = \frac{1}{C_\ell} (\bar{q}_{11} - \bar{q}_{12})$$

The cross-sectional areas of the two lines are assumed to be equal ( $A_1 = A_2 = A$ ); thus the compliance per lump is

$$C_\ell = \frac{gA\ell}{\rho a^2}$$

where  $g$  is the gravitational constant,  $\rho$  is the liquid-oxygen density,  $a$  is the speed of sound in liquid oxygen,  $L_\ell (= \rho\ell / Ag)$  is the inertance per lump,  $R_\ell$  is the resistance per lump, and  $P_{tb}$  is the tank-base pressure.

The equation for the pressure at the inlet to the LPOP can be written by considering the cavitation bubble compliance and the motions of the elbow and LPOP (station locations 3 and 4 in fig. 26) as they affect the fluid system. The result is

$$\dot{p}_{12} \triangleq \dot{P}_4 = (Q_4 - Q_5) + \frac{A_2}{C_{b1}} (\dot{x}_4 - \dot{x}_3) + \frac{A_3}{C_{b1}} \dot{z}_4 - \frac{A_2}{C_{b1}} \dot{z}_3$$

where  $C_{b1}$  is the cavitation bubble compliance and  $A_3$  is the LPOP exit area, which equals the interpump duct area. The equations for the interpump duct were written for the duct as one lump with resistance  $R_1$ , inertance  $L_1$ , and cavitation compliance  $C_{b2}$  at the HPOP inlet. The resulting equations are

$$\dot{Q}_5 = \frac{1}{L_1 + L_{p1}} \left[ (m_1 + 1)P_4 - P_7 - (R_1 + R_{p1})Q_5 + R_{p1}A_3\dot{z}_4 + R_1A_3\dot{z}_7 \right]$$

$$P_5 = (m_1 + 1)P_4 - R_{p1}Q_5 - L_{p1}\dot{Q}_5 + R_{p1}A_3\dot{z}_4$$

$$\dot{P}_7 = \frac{1}{C_{b1}} \left[ Q_5 - Q_{tc} + Q_a + Q_{d7} + (A_4 - A_3)\dot{z}_7 \right]$$

where  $L_{p1}$  is the LPOP inertance,  $m_1 + 1$  is the LPOP gain,  $R_{p1}$  is the LPOP resistance,  $Q_a$  is the suppressor flow rate (at the HPOP inlet),  $Q_{d7}$  is the flow disturbance at the HPOP inlet, and  $A_4$  is the HPOP suction area. All parameters associated with the pumps and the interpump duct were obtained from references 2 and 4.

The equations for the discharge line and thrust chamber pressure  $P_{tc}$  and flow  $Q_{tc}$ , which complete the propulsion system model, can be written as

$$\dot{Q}_{tc} = \frac{1}{L_d + L_J + L_{p2}} \left[ P_7 - P_{tc} - (R_d + R_J + R_{p2})Q_{tc} + A_4 \dot{z}_7 \right]$$

and

$$P_{tc} = \frac{R_{tc}}{\tau_{tc}} \left( Q_{tc} - \frac{P_{tc}}{R_{tc}} - A_4 \dot{z}_7 \right)$$

where the following parameters were also obtained from references 2 and 4:  $L_d$ , the discharge line inertance;  $L_J$ , the injector inertance;  $L_{p2}$ , the HPOP inertance;  $R_d$ , the discharge line resistance;  $R_J$ , the injector resistance;  $R_{p2}$ , the HPOP resistance;  $R_{tc}$ , the thrust chamber resistance; and  $\tau_{tc}$ , the thrust chamber time constant.

### Structural Dynamic Equations

In the model, seven structural elements characterize the liquid-oxygen system. The primary structural output quantities of interest are the horizontal  $\dot{z}$  and vertical  $\dot{x}$  velocities of each element. The structural elements and their associated indexes are tb, tank base;  $\ell 1$ , vertical feedline; 1, first elbow;  $\ell 2$ , horizontal feedline; 3, second elbow; 4, LPOP; and 7, the interpump duct - HPOP - discharge line - thrust chamber combination.

The structural model was developed as in references 2 and 4 except for the treatment of feedline drag forces. The modal equations can be written as

$$M_n \left( \ddot{q}_n + 2\zeta_n \omega_n \dot{q}_n + \omega_n^2 q_n \right) = \mathcal{F}_n \quad n = 1, 2, \dots, 6$$

where, for the  $n^{\text{th}}$  mode,  $M_n$  is the generalized mass,  $q_n$  is the generalized displacement,  $\zeta_n$  is the damping ratio,  $\omega_n$  is the natural frequency, and  $\mathcal{F}_n$  is the generalized force.

The model in references 2 and 4 has six modes, which are assumed to adequately describe the system at a particular flight condition. In this model the structural velocities  $\dot{x}_i$  and  $\dot{z}_i$  can be related to the six generalized velocities  $\dot{q}_n$  by

$$\dot{x}_i = \sum_{n=1}^6 \varphi_n^{(x)}(i) \dot{q}_n \quad i = \ell 1, 1, 3, 4, 7, \text{tb}$$

$$\dot{z}_i = \sum_{n=1}^5 \varphi_n^{(z)}(i) \dot{q}_n \quad i = \ell 2, 1, 3, 4, 7$$

where  $\varphi_n^{(x)}(i)$  and  $\varphi_n^{(z)}(i)$  are components of the mode shape vectors. For example, the  $n^{\text{th}}$  mode shape vector  $\Phi_n$  is written as

$$\Phi_n = \begin{bmatrix} \varphi_n^{(x)}(\ell 1) \\ \varphi_n^{(x)}(1) \\ \varphi_n^{(x)}(3) \\ \varphi_n^{(x)}(4) \\ \varphi_n^{(x)}(7) \\ \varphi_n^{(x)}(\text{tb}) \\ \varphi_n^{(z)}(\ell 2) \\ \varphi_n^{(z)}(1) \\ \varphi_n^{(z)}(3) \\ \varphi_n^{(z)}(4) \\ \varphi_n^{(z)}(7) \end{bmatrix}$$

where the ordering of structural velocities is arbitrary. The remaining structural output (tank pressure) can be related to the generalized accelerations, as shown in references 2 and 4, as

$$P_{\text{tb}} = \sum_{i=1}^6 \mathcal{P}_i(\text{tb}) \ddot{q}_i$$

where coefficients  $\mathcal{P}_i(\text{tb})$  are given.

The generalized force on the  $n^{\text{th}}$  mode was shown in references 3 and 5 to be

$$\mathcal{F}_n = \mathcal{P}_n(\text{tb}) \left[ \dot{\bar{q}}_1 + A_1 \sum_{k=1}^6 \ddot{q}_k \varphi_k^{(x)}(\text{tb}) \right] + P_{\text{tb}} A_1 \varphi_n^{(x)}(\text{tb}) + \sum_i F_i^{(x)} \varphi_n^{(x)}(i) + \sum_j F_j^{(z)} \varphi_n^{(z)}(j)$$

where

$$i = \ell 1, 1, 3, 4, 7, \text{tb}$$

$$j = \ell 2, 1, 3, 4, 7$$

$$n = 1, 2, \dots, 6$$

The first term accounts for forces generated by liquid-oxygen-tank outflow and the second accounts for forces generated by tank pressure variation. The terms  $F_1^{(x)}$  and  $F_j^{(z)}$  are the actual forces on the structure due to flow rate, pressure, and structural velocities at the seven defined locations. These forces are made up of (1) drag forces on the feedlines, the interpump duct, and the discharge line; (2) momentum forces at the two feedline corners, the LPOP, and the HPOP; and (3) forces on the thrust chamber.

In a manner like that used in references 2 and 4, these forces can be expressed in terms of flows, pressures, and structural velocities previously defined:

(1) Vertical and horizontal feedlines: The modeling here differs from that in references 2 and 4 since the feedline models are lumped instead of distributed. The drag forces are

$$F_{\ell 1}^{(x)} = -A_1 R_{\ell} \left( \sum_{i=1}^9 \bar{q}_i + A_1 \dot{x}_{\ell 1} \right)$$

$$F_{\ell 2}^{(z)} = A_2 R_{\ell} \left( \sum_{i=10}^{12} \bar{q}_i - A_2 \dot{z}_{\ell 2} \right)$$

(2) First elbow:

$$F_1^{(x)} = -P_2 A_1 - \bar{f} \left( 2 \frac{Q_1}{A_1} + \dot{x}_1 \right)$$

$$F_1^{(z)} = -P_2 A_2 - \bar{f} \left( 2 \frac{Q_2}{A_2} - \dot{z}_1 \right)$$

(3) Second elbow:

$$F_z^{(x)} = P_4 A_2 + \bar{f} \left( 2 \frac{Q_4}{A_2} + \dot{x}_3 \right)$$

$$F_3^{(z)} = P_4 A_2 + \bar{f} \left( 2 \frac{Q_4}{A_2} + \dot{z}_3 + 2\dot{x}_3 \right)$$

(4) LPOP:

$$F_4^{(x)} = -P_4 A_2 - \bar{f} \left( 2 \frac{Q_4}{A_2} + \dot{x}_4 \right)$$

$$F_4^{(z)} = -P_5 A_3 - \bar{f} \left( 2 \frac{Q_5}{A_3} - \dot{z}_4 \right)$$

(5) Interpump duct - HPOP - discharge line - thrust chamber:

$$F_7^{(x)} = A_{tc} c_f P_{tc}$$

$$F_7^{(z)} = A_3 R_I (Q_7 - A_3 \dot{z}_7) + A_4 R_d (Q_{tc} - A_4 \dot{z}_7) + P_7 A_3 - P_c A_4 + 2\bar{f} \left( \frac{Q_7}{A_3} - \frac{Q_{tc}}{A_4} \right) + A_4 P_{tc}$$

Here,  $\bar{f}$  is the mean mass flow of the liquid oxygen,  $A_{tc}$  is the thrust chamber area, and  $c_f$  is the discharge coefficient.

### Suppressor Dynamics

The suppressor piston actuator is modeled as a first-order lag process with the transfer function

$$Q_a(s) = \frac{\omega_a}{s + \omega_a} u_a(s)$$

where  $u_a(s)$  is the commanded flow input that produces the desired output suppressor flow rate  $Q_a(s)$ .

## Expressing Model in State-Variable Form

The linear quadratic regulator approach to pogo suppressor design requires that a state-variable model of the standard form

$$\dot{x} = Ax + Bu + Dw$$

$$y = Hx$$

be obtained for the liquid-oxygen system. To do this, first a 12th-order structural system state vector  $x_s$  is defined as made up of modal displacements and velocities.

$$x_s^T \triangleq (q_1, \dot{q}_1, q_2, \dot{q}_2, \dots, q_6, \dot{q}_6)$$

Then a 29th-order propulsion system state vector  $x_p$  is defined as

$$x_p^T \triangleq (\bar{q}_1, p_1, \bar{q}_2, p_2, \bar{q}_3, p_3, \bar{q}_4, p_4, \bar{q}_5, p_5, \bar{q}_6, p_6, \bar{q}_7, p_7,$$

$$\bar{q}_8, p_8, Q_1, P_1, Q_2, P_2, \bar{q}_{11}, p_{11}, Q_4, P_4, Q_5, P_5, Q_{tc}, Q_a)$$

Note here that suppressor flow rate  $Q_a$  is included as part of the propulsion system state vector.

For convenience in forming a state-variable model, the following vectors are defined:

$$v_s^T \triangleq (\mathcal{F}_1, \mathcal{F}_2, \dots, \mathcal{F}_6) \quad \text{6th-order vector of generalized forces}$$

$$y_s^T \triangleq (\dot{x}_{l1}, \dot{x}_1, \dot{x}_3, \dot{x}_4, \dot{x}_7, \dot{x}_{tb}, \dot{z}_{l2}, \dot{z}_1, \dot{z}_3, \dot{z}_4, \dot{z}_7, \mathcal{P}_{tb})$$

12th-order vector of structural-system outputs

Also, the system disturbance  $w$  is selected as flow-rate disturbance  $Q_{d7}$ . (Tank pressure  $P_{tb}$  is considered to be a structural output.) With these definitions, state-variable equations can be written for the structural system as

$$\dot{x}_s = A_s x_s + E_s v_s$$

$$y_s = C_s x_s + \bar{C}_s \dot{x}_s$$

$$v_s = F_s y_s + D_{sp} x_p + F_q \dot{x}_s$$

by using the equations appearing on pages 35 to 40. Matrices  $A_s$ ,  $E_s$ ,  $C_s$ ,  $\bar{C}_s$ ,  $F_s$ ,  $D_{sp}$ , and  $F_q$  are given in table VI.

For the propulsion system, state equations can be written as

$$\dot{x}_p = A_p x_p + B_p u + D_{ps} y_s + D_p w$$

where matrices  $A_p$ ,  $B_p$ ,  $D_p$ , and  $D_{ps}$  are given in table VII.

Because of the  $\dot{x}_s$  terms on the right sides of the structural state equations, the equations are not yet in "standard" state-variable form. However, by a straightforward but lengthy substitution process, the state-variable equations

$$\dot{x}_s = \bar{A}_s x_s + \bar{B}_s x_p$$

$$\dot{x}_p = \bar{A}_p x_p + \bar{B}_p x_s + B_p u + D_p w$$

$$y_s = H_p x_p + H_s x_s$$

can be obtained, where the following matrices are defined:

$$\bar{A}_s \triangleq A_s + E_s U (F_s W_1 + F_q A_s)$$

$$\bar{A}_p \triangleq A_p + D_{ps} W_2$$

$$\bar{B}_s \triangleq E_s U (F_s W_2 + D_{sp})$$

$$\bar{B}_p \triangleq D_{ps} W_1$$

$$H_p \triangleq V \bar{C}_s E_s (I + F_q E_s) D_{sp}$$

$$H_s \triangleq V \left\{ C_s + \bar{C}_s \left[ I + E_s F_q (I + E_s U F_q) \right] A_s \right\}$$

and the following intermediate matrices are defined:

$$U \triangleq (I - F_q E_s)^{-1}$$

$$V \triangleq \left[ I - \bar{C}_s E_s (I + F_q E_s U) F_s \right]^{-1}$$

$$W_1 \triangleq V \left[ C_s + \bar{C}_s (I + E_s F_q + E_s F_q E_s U F_q) A_s \right]$$

$$W_2 \triangleq C_s E_s (I + F_q E_s U) D_{sp}$$

### Colored-Noise Disturbance

A second-order, colored-noise process, with natural frequency  $\omega_{cn}$  and damping  $\zeta_{cn}$ , was chosen to model the disturbance  $w$ . The state equations for this coloring can be written as

$$\begin{pmatrix} \dot{x}_{cn1} \\ \dot{x}_{cn2} \end{pmatrix} = \begin{bmatrix} 0 & 1 \\ -\omega_{cn}^2 & -2\zeta_{cn}\omega_{cn} \end{bmatrix} \begin{pmatrix} x_{cn1} \\ x_{cn2} \end{pmatrix} + \begin{bmatrix} 0 \\ 1 \end{bmatrix} w$$

$$w_{cn} = \begin{bmatrix} \omega_{cn}^2 & 0 \end{bmatrix} \begin{pmatrix} x_{cn1} \\ x_{cn2} \end{pmatrix}$$

or

$$\dot{x}_{cn} = A_{cn} x_{cn} + D_{cn} w$$

$$w_{cn} = H_{cn} x_{cn}$$

Here,  $w$  is considered to be a white-noise disturbance.

### Overall State Equations

Finally, by defining a 43rd-order overall state vector and a 12th-order output vector as

$$x \triangleq \begin{pmatrix} x_p \\ \text{---} \\ x_s \\ \text{---} \\ x_{cn} \end{pmatrix}; \quad y \triangleq y_s; \quad u \triangleq u_a$$

the desired overall state equation becomes

$$\dot{\bar{x}} = A\bar{x} + Bu + Dw$$

$$y = H\bar{x}$$

where

$$A \triangleq \begin{bmatrix} \bar{A}_p & | & \bar{B}_p & | & D_p H_{cn} \\ \hline \bar{B}_s & | & \bar{A}_s & | & 0 \\ \hline 0 & | & 0 & | & A_{cn} \end{bmatrix}$$

$$B \triangleq \begin{bmatrix} B_p \\ \hline 0 \\ \hline 0 \end{bmatrix}$$

$$D \triangleq \begin{bmatrix} 0 \\ \hline 0 \\ \hline D_{cn} \end{bmatrix}$$

$$H \triangleq \begin{bmatrix} H_p & | & H_s & | & 0 \end{bmatrix}$$

### Parameter Values

The nominal parameters that characterize the propulsion system are given in table I. Except for line inertance and compliance and actuator frequency, all were obtained from references 2 and 4.

Bubble compliances  $C_{b1}$  and  $C_{b2}$  and pump gains  $m_1 + 1$  and  $m_2 + 1$  are especially dependent on flight condition. The values shown in table I define the expected parameter ranges. Structural parameters required are mainly the modal vector data plus modal frequencies, masses, and damping ratios. Table II presents these data, which are adapted from data in references 2 and 4, for the two flight conditions of

interest - end burn and after solid-rocket separation. These two conditions were chosen because preliminary analysis showed their pogo instabilities to be most pronounced.

#### Nominal Worst-Case Model

A nominal worst-case model was developed to reflect the dynamics of the two most critical flight conditions - end burn and after solid-rocket separation - and to achieve an open-loop model of the more unstable condition. The worst-case model is basically the reference 2 model at end burn except that the end-burn structural mode at 2.81 hertz (E1) was replaced by a less stable mode (A1) from the after-separation condition (table II). The frequency of the fifth end-burn mode was shifted from 26.8 hertz to 23.8 hertz, making the system open-loop unstable. Also, the LPOP and HPOP gains were set to the maximum values shown in table I, and the pump inlet bubble compliances were set to the minimum values shown in table I.

# APPENDIX C

## LISTING OF SUBROUTINE POGMAT

Subroutine POGMAT is written in FORTRAN and performs the necessary matrix manipulations to calculate matrices A, B, D, and H given, as data, the parameters listed in table I and the structural information contained in tables VI and VII.

```

0000100      SUBROUTINE POGMAT(IDEU3)
0000200 C      THIS SUBROUTINE CALCULATES THE A,B,C,HH,AND D MATRICES FOR THE 41ST ORDER
0000300 C      POGO PROBLEM. ALSO,DIMENSIONS N,NM,NC,ND,NO,AND NU ARE INPUT FROM POGMAT
0000400 C      TO THE MAIN PROGRAM.
0000500      IMPLICIT REAL*8 (A-H,O-3,U-Z)
0000500      REAL*8 T, TAUC, TAUCR, TAUP, TEMPB, TEMPC, TS, TSPTR, PST, PT
0000700      REAL*8 L, ICONST, LL, NN, NC, KC, LLR, LI, LP1, LD, LJ, LP2, LILPR, -
0000800      1 KE, LDJP2, LPA
0000900      COMMON /ABETC/ A(50,50), B(50,50), C(50,50), D(50,15), HH(5,50), -
0001000      1 QC(50,50), NN(50,5), PCINV(5,5), QO(50,50), RRINV(5,5)
0001100      COMMON /COM1/ ADBLE(2500), EX1(50,50), EX2(50,50), EX3(50,50), -
0001200      1 EX4(50), EX1(100,100), KC(2,50), AMBKC(50,50), ANR(50), ANI(50), -
0001300      2 EIGR(50), EIGI(50), X(100,100), EIGCLR(50), EIGCLI(50), TS2(10), -
0001400      3 AR(100), AI(100), XR(100,100), PT(100,100), AAA(100,100), -
0001500      4 CR(100), CI(100), S(50,50), SS(50,50), SSS(50,50), FREQ(500), -
0001600      5 AMP(500), PHASE(500), AMP1(500), PHA1(500), AMP2(500), PHA2(500), -
0001700      6 AMPSTR(1000), PHASTR(1000), AINV(50,50), AMBINV(50,50), -
0001800      7 ABKHIN(50,50), ABKCEH(50,50), IBL(100), IA(100), IB(100), -
0001900      8 LEX(100), MEX(100), KE(50,5), PP(50,50), XTIME(1000), U(1000), -
0001920      9 EX5(50,2), EX6(5,50)
0002000      COMMON/COM2/ AP(30,30), BP(30,2), DPS(30,20), CP(30,30), -
0002100      1 AS(20,20), ES(20,10), DS(20,15), CS(20,20), FS(10,20), FP(10,2), -
0002200      2 DSP(10,30), FE(10), DP(30,15), ZE(10)
0002400      COMMON/COM3/ CUSYS(2,5), CUU(2,50), BU(50,50), AU(50,50), -
0002500      1 CTOF(100,100), DFOT(100,15), XOLD(100), XNEW(100), TEMPC(2,50), -
0002600      2 TEMPB(50,50), ATOF(100,100)
0002700      COMMON/DIMS/N, NM, NC, ND,NO, NU, N2
0002800      COMMON /STRUCT/ NS, NP
0002900      NAMELIST/PARIN/ RP1, CB1, CB2, BSFAR, AREA, AREA1, AREA2, AREA3, -
0003000      1 AREA4, L, RHO, G, RL, RI, RD, RC, RJ, RP2, LI, LP1, LD, LJ, LP2, -
0003100      2 PM1, PM2, R3, R4, TAUC, FBAR, ATCF, N, NM, NU, NS, NSO, NSP, NPJ, -
0003200      3 NC, ND, CS, FE, ZE, ES, WA, SPDSND,IACT,AP7,IAS
0003220 C
0003240 C***** DATA *****
0003260 C
0003300      IAS = 0
0003400      WRITE (2,2025)
0003500      READ (2,4568) IAS
0003600      WRITE (2,4580)
0003700      READ (2,4568) IACT
0003800 4568  FORMAT(I1)
0003900 55  CONTINUE
0004000      RP1 = .021424D0
0004100      CB1 = .25D0
0004200      CB2 = .10D0
0004300      AREA = 75.7D0
0004400      AREA1 = 75.7D0
0004500      AREA2 = 75.7D0
0004600      L = 136.0D0
0004700      RHO = .03813D0
0004800      G = 386.4D0
0004900      BSTAR = 2.434D-5
0005000      RL = 9.85D-5
0005100      WA = 314.16D0
0005200      RC = .103D0
0005300      RI = .004532D0
0005400      RD = .020188D0
0005500      RJ = .146672D0
0005600      RP2 = .108768D0

```

```

0005700      LI = .5356D-3
0005800      LP1 = .412D-4
0005900      LD = .618D-3
0006000      LJ = .206D-3
0006100      LP2 = .103D-3
0006200      PM1 = .306D0
0006300      PM2 = .42D0
0006400      TAUC = .45D-3
0006500      ESALL = 1.0D0 / 232.0D0
0006500      R4 = .020188D0
0006700      R3 = .004532D0
0006800      IF (IAS .NE. 1) GO TO 4500
0006900      PM1 = .80D0
0007000      PM2 = .54D0
0007100      CB1 = 1.0D0
0007200      CB2 = .110D0
0007300 4500 CONTINUE
0007400      N = 41
0007500      NM = 1
0007600      NS = 12
0007700      NSO = 12
0007800      NSF = 6
0007900      NP = 29
0008000      NPO = 29
0008100      NC = 1
0008200      ND = 1
0008300      NMAX = 50
0008400      NMMAX = 5
0008500      NPMAX = 30
0008600      NPOMAX = 30
0008700      NSMAX = 20
0008800      NSOMAX = 20
0008900      NSFMAX = 10
0009000      NCMAX = 5
0009100      NDMAX = 15
0009200      NOMAX = 50
0009300      N2MAX = 100
0009400      N2 = N + N
0009500      NO=NSO+NPO
0009600      NTOT=N+NU
0009700      DO 4502 J = 1,N
0009800      DO 4502 I = 1,NM
0009900 4502  HH(I,J) = 0.0D0
0010000      DO 2001 J = 1,NS
0010100      DO 2001 I = 1,NSO
0010200 2001  CS(I,J) = 0.0D0
0010300      DO 2002 J = 1,NSO
0010400      DO 2002 I = 1,NP
0010500 2002  DPS(I,J) = 0.0D0
0010600      DO 2003 J = 1,NSF
0010700      DO 2003 I = 1,NS
0010800 2003  ES(I,J) = 0.0D0
0010900      DO 2004 J = 1,NPO
0011000      DO 2004 I = 1,NSF
0011100 2004  DSP(I,J) = 0.0D0
0011200      DO 2005 J = 1,NP
0011300      DO 2005 I = 1,NPO
0011400 2005  CP(I,J) = 0.0D0
0011500      DO 2006 J = 1,NS
0011600      DO 2006 I = 1,NS
0011700 2006  AS(I,J) = 0.0D0
0011800      DO 2007 J = 1,NSO
0011900      DO 2007 I = 1,NSF
0012000 2007  FS(I,J) = 0.0D0
0012100      DO 2008 J = 1,NP
0012200      DO 2008 I = 1,NP
0012300 2008  AP(I,J) = 0.0D0
0012400      DO 2009 J = 1,NC
0012500      DO 2009 I = 1,NSF
0012600 2009  FP(I,J) = 0.0D0
0012700      DO 2021 J = 1,NC
0012800      DO 2021 I = 1,NP
0012900 2021  EP(I,J) = 0.0D0
0013000      DO 2022 J = 1,ND

```

0013100		DO 2022 I = 1,NP
0013200	2022	DP (I,J) = 0.0D0
0013300		DO 2023 J = 1,ND
0013400		DO 2023 I = 1,NS
0013500	2023	DS (I,J) = 0.0D0
0013600		CS (1,2) = - .156D0
0013700		CS (2,2) = - .33D0
0013800		CS (3,2) = - .33D0
0013900		CS (4,2) = .255D0
0014000		CS (5,2) = .255D0
0014100		CS (6,2) = - .209D0
0014200		CS (7,2) = .0367D0
0014300		CS (8,2) = .0367D0
0014400		CS (9,2) = .0357D0
0014500		CS (10,2) = .846D0
0014600		CS (11,2) = .846D0
0014700		IF (IAS .NE. 1) GO TO 2026
0014800		CS (1,2) = .529D0
0014900		CS (2,2) = .208D0
0015000		CS (3,2) = .208D0
0015100		CS (4,2) = 1.28D0
0015200		CS (5,2) = 1.28D0
0015300		CS (6,2) = .257D0
0015400		CS (7,2) = .094D0
0015500		CS (8,2) = .094D0
0015600		CS (9,2) = .094D0
0015700		CS (10,2) = 1.68D0
0015800		CS (11,2) = 1.68D0
0015900		CS (12,2) = - 2.16D-3
0016000	2026	CONTINUE
0016100		CS (1,4) = - .198D0
0016200		CS (2,4) = - .245D0
0016300		CS (3,4) = - .245D0
0016400		CS (4,4) = .239D0
0016500		CS (5,4) = .239D0
0016600		CS (6,4) = - .334D0
0016700		CS (7,4) = - .352D0
0016800		CS (8,4) = - .352D0
0016900		CS (9,4) = - .352D0
0017000		CS (10,4) = .50D0
0017100		CS (11,4) = .50D0
0017200		CS (1,6) = .054D0
0017300		CS (2,6) = - .0787D0
0017400		CS (3,6) = - .0787D0
0017500		CS (4,6) = - .556D0
0017600		CS (5,6) = - .556D0
0017700		CS (6,6) = - .259D0
0017800		CS (7,6) = .431D0
0017900		CS (8,6) = .431D0
0018000		CS (9,6) = .431D0
0018100		CS (10,6) = - 1.95D0
0018200		CS (11,6) = - 1.95D0
0018300		CS (1,8) = .022D0
0018400		CS (2,8) = - .752D0
0018500		CS (3,8) = - .752D0
0018600		CS (4,8) = - 1.71D0
0018700		CS (5,8) = - 1.71D0
0018800		CS (6,8) = - 7.74D0
0018900		CS (7,8) = - .372D0
0019000		CS (8,8) = - .372D0
0019100		CS (9,8) = - .372D0
0019200		CS (10,8) = - .12D0
0019300		CS (11,8) = - .12D0
0019400		CS (1,10) = .222D0
0019500		CS (2,10) = .37D0
0019600		CS (3,10) = .37D0
0019700		CS (4,10) = - 2.13D0
0019800		CS (5,10) = - 2.13D0
0019900		CS (6,10) = 4.443D0
0020000		CS (7,10) = .017D0
0020100		CS (8,10) = .017D0
0020200		CS (9,10) = .017D0
0020300		CS (10,10) = .99D0
0020400		CS (11,10) = .99D0

```

0020500 CS(1,12) = .022D0
0020600 CS(2,12) = .0134D0
0020700 CS(3,12) = .0134D0
0020800 CS(4,12) = 2.63D0
0020900 CS(5,12) = 2.63D0
0021000 CS(6,12) = 5.336D0
0021100 CS(7,12) = - .09D0
0021200 CS(8,12) = - .09D0
0021300 CS(9,12) = - .09D0
0021400 CS(10,12) = - 1.56D0
0021500 CS(11,12) = - 1.56D0
0021600 FE(1) = 2.81D0
0021700 FE(2) = 4.73D0
0021900 FE(3) = 8.49D0
0021900 FE(4) = 22.5D0
0022000 FE(5) = 26.8D0
0022100 FE(6) = 24.0D0
0022200 ZE(1) = .01D0
0022300 ZE(2) = .01D0
0022400 ZE(3) = .01D0
0022500 ZE(4) = .01D0
0022600 ZE(5) = .01D0
0022700 ZE(6) = .01D0
0022800 FBAR = 2.29D0
0022900 ATCF = 158.0D0
0023000 AREA3 = 31.2D0
0023100 AREA4 = 12.6D0
0023200 AREAP = AREA3
0023300 AP7 = - .148D-2
0023400 4589 CONTINUE
0023500 IF (IAS .NE. 1) GO TO 5000
0023600 FE(1) = 2.3D0
0023700 5000 CONTINUE
0023720 C
0023740 C*****
0023760 C
0023800 CL = BSTAR * AREA * L
0023900 LL = RHO * L / G / AREA
0024000 ROL = RL / LL
0024100 CLR = 1.0D0 / CL
0024200 LLR = 1.0D0 / LL
0024300 RAL = RL * AREA / LL
0024400 CB1R = 1.0D0 / CB1
0024500 CB2R = 1.0D0 / CB2
0024600 LILPR = 1.0D0 / (LI + LP1)
0024700 LDJP2 = LD + LJ + LP2
0024800 TAUCR = 1.0D0 / TAUC
0024900 A6 = (RD + RJ + RP2) / LDJP2
0025000 ARM1 = AREA1 * RL
0025100 ARM2 = AREA2 * RL
0025200 AR3 = AREA3 * R3
0025300 A32R = AR3 * AREA3
0025400 A12R = AREA1 * AREA1 * RL
0025500 A22R = AREA2 * AREA2 * RL
0025600 FBA1 = 2.0D0 * FBAR / AREA1
0025700 FBA2 = 2.0D0 * FBAR / AREA2
0025800 FBA3 = 2.0D0 * FBAR / AREA3
0025900 FBA4 = 2.0D0 * FBAR / AREA4
0026000 PML1B = (1.0D0 + PM1) * LI * LILPR * AREA3
0026100 RLMRL = (RI * LP1 - RP1 * LI) * LILPR * AREA3
0026200 RLMRL = - RLMRL
0026300 LPA = LP1 * LILPR * AREA3
0026400 APM2 = AREA4 * (PM2 + 1.0D0)
0026500 RA3L = RP1 * AREA3 * AREA3 * LI * LILPR
0026600 RLA3 = RI * LP1 * AREA3 * AREA3 * LILPR
0026700 A26B = APM2 * (LJ / LDJP2 - 1.0D0 + LP2 / LDJP2) + AREA3
0026800 A27B = AREA4 * (-LP2 * A6 + RP2 + RJ - LJ * A6 + R4) - FBA4
0026900 A28B = AREA4 * (-LP2 / LDJP2 + 1.0D0 - LJ / LDJP2)
0027000 F10B = FBAR - RA3L
0027100 F11B = AREA4 * AREA4 * (LJ * A6 - RJ + LP2 * A6 - R4 - RP2) - A32R
0027200 DO 1 J=1,N
0027300 DO 101 I=1,NC
0027400 101 B(J,I) = 0.0D0
0027500 DO 102 I = 1,ND

```

```

0027600 102 D(J,I) = 0.000
0027700 DO 1 I = 1,N
0027800 A(I,J) = 0.000
0027900 C(I,J) = 0.000
0028000 IF (I .EQ. J) C(I,J) = 1.000
0028100 1 CONTINUE
0028200 BP(29,1) = WA
0028300 IF (IACT .NE. 2) GO TO 3
0028400 BP(25,1) = - WA * LI * LILPR
0028500 8 CONTINUE
0028600 D(28,1) = RC / TAUC
0028700 DO 4 I=1,21,2
0028800 AP(I+1,I) = CLR
0028900 AP(I+2,I+1) = LLR
0029000 AP(I,I+1) = - LLR
0029100 AP(I+1,I+2) = - CLR
0029200 4 AP(I,I) = - ROL
0029300 AP(23,23) = - ROL
0029400 AP(23,24) = - LLR
0029500 AP(24,23) = CB1R
0029600 AP(24,25) = - CB1R
0029700 AP(25,24) = LILPR * (PM1 + 1.000)
0029800 AP(25,25) = - (RI + RP1) * LILPR
0029900 AP(25,26) = - LILPR
0030000 AP(26,25) = CB2R
0030100 AP(26,27) = - CB2R
0030200 AP(27,26) = (PM2 + 1.000) / LDJP2
0030300 AP(27,27) = - (RD + RJ + RP2) / LDJP2
0030400 AP(27,28) = - 1.000 / LDJP2
0030500 AP(28,27) = RC * FAUCR
0030600 AP(28,28) = - TAUCR
0030700 AP(29,29) = - WA
0030800 C
0030900 IF (IACT .NE. 1) GO TO 5
0031000 AP(24,29) = CB1R
0031100 5 IF (IACT .NE. 2) GO TO 5
0031200 AP(25,29) = - LILPR * (RI - WA * LI)
0031300 6 IF (IACT .NE. 2 .AND. IACT .NE. 3) GO TO 7
0031400 AP(26,29) = CB2R
0031500 7 CONTINUE
0031500 C
0031700 DO 2010 J = 1,NP
0031800 DO 2010 I = 1,NP
0031900 2010 A(I,J) = AP(I,J)
0032000 DO 2110 J = 1,NC
0032100 DO 2110 I = 1,NP
0032200 2110 B(I,J) = BP(I,J)
0032300 AP(29,26) = - 1.00-8
0032400 DO 3001 I = 1,17,2
0032500 3001 DPS(I,1) = - RAL
0032600 DPS(18,2) = AREA * CLR
0032700 DPS(24,3) = - AREA * CB1R
0032800 DPS(24,4) = - DPS(24,3)
0032900 DPS(19,7) = RAL
0033000 DPS(21,7) = RAL
0033100 DPS(23,7) = RAL
0033200 DPS(18,8) = DPS(18,2)
0033300 DPS(24,9) = DPS(24,3)
0033400 DPS(24,10) = AREA3 * CB1R
0033500 DPS(25,10) = RP1 * AREA3 * LILPR
0033600 DPS(25,11) = RI * AREA3 * LILPR
0033700 DPS(26,11) = (AREA4 - AREA3) * CB2R
0033800 DPS(27,11) = AREA4 * A5
0033900 DPS(28,11) = - RC * AREA4 * TAUCR
0034000 DPS(1,12) = LLR
0034100 DO 3003 J = 1,NS
0034200 JJ = NP + J
0034300 DO 3003 I = 1,NP
0034400 SUM = 0.000
0034500 DO 3002 K = 1,NSO
0034600 3002 SUM = SUM + DPS(I,K) * CS(K,J)
0034700 3003 A(I,JJ) = SUM
0034800 DO 3004 I = 2,NS,2
0034900 J = I / 2

```

```

0035000 3004 ES(I,J) = ESALL
0035100 ES(12,6) = 2.200 / 292.000
0035200 IF (IAS .NE. 1) GO TO 3100
0035300 ES(2,1) = 1.000/1232.000
0035400 3100 CONTINUE
0035500 DO 3005 I = 1,NSF
0035600 K = 2 * I
0035700 3005 DSP(I,1) = - ARM1 * CS(1,K)
0035800 DO 3006 J = 3,17,2
0035900 DO 3006 I = 1,NSF
0036000 3006 DSP(I,J) = DSP(I,1)
0036100 DO 3007 I = 1,NSF
0036200 K = 2 * I
0036300 DSP(I,1) = DSP(I,1) + CS(12,K)
0036400 DSP(I,17) = DSP(I,17) - PBA1 * CS(2,K)
0036500 DSP(I,18) = - AREA1 * CS(2,K) - AREA2 * CS(8,K)
0036600 PS(I,1) = - A12B * CS(1,K)
0036700 PS(I,2) = - PBAR * CS(2,K)
0036800 PS(I,3) = PRAR * CS(3,K) + 2.000 * FBAR * CS(9,K)
0036900 PS(I,4) = - PBAR * CS(4,K)
0037000 PS(I,6) = AREA1 * CS(12,K)
0037100 PS(I,7) = - A22F * CS(7,K)
0037200 PS(I,8) = PBAR * CS(8,K)
0037300 PS(I,9) = PBAR * CS(9,K)
0037400 PS(I,10) = F10B * CS(10,K)
0037500 PS(I,11) = RLA3 * CS(10,K) + F11B * CS(11,K)
0037600 3007 PS(I,12) = AREA1 * CS(5,K)
0037700 DO 3009 J = 19,23,2
0037800 DO 3009 I = 1,NSF
0037900 K = 2 * I
0038000 3009 DSP(I,J) = ARM2 * CS(7,K)
0038100 DO 3010 I = 1,NSF
0038200 K = 2 * I
0038300 DSP(I,19) = DSP(I,19) - PBA2 * CS(8,K)
0038400 EX4(I) = CS(3,K) - CS(4,K) + CS(9,K)
0038500 DSP(I,23) = DSP(I,23) + PBA2 * EX4(I)
0038600 DSP(I,24) = AREA2 * EX4(I) - PML1B * CS(10,K)
0038700 DSP(I,25) = CS(10,K) * (RLMRL - PBA3) + CS(11,K) * (AR3 + PBA3)
0038800 DSP(I,26) = - CS(10,K) * LPA + CS(11,K) * A25B
0038900 DSP(I,27) = CS(11,K) * A27B
0039000 3010 DSP(I,28) = CS(11,K) * A23B + CS(5,K) * ATPC
0039100 IF (IACT .NE. 2) GO TO 3050
0039200 DO 3040 I = 1,NSF
0039300 K = I * 2
0039400 DO 3035 J = 1,NC
0039500 3035 PP(I,J) = - LP1 * LI * WA * LILPR * AREA3 * CS(10,K)
0039600 3040 DSP(I,29) = (PBA3 + AR3) * CS(11,K) - LP1 * LILPR * (RI - WA * LI) -
0039700 1 * AREA3 * CS(10,K)
0039800 3050 CONTINUE
0039900 DO 3011 J = 1,NP
0040000 DO 3011 I = 1,NPO
0040100 CP(I,J) = 0.000
0040200 IF (I .EQ. J) CP(I,J) = 1.000
0040300 3011 CONTINUE
0040400 DO 3013 J = 1,NP
0040500 DO 3013 I = 1,NS
0040600 II = NP + I
0040700 SUM = 0.000
0040800 DO 3012 K = 1,NPO
0040900 DO 3012 IL = 1,NSF
0041000 3012 SUM = SUM + ES(I,IL) * DSP(IL,K) * CP(K,J)
0041100 3013 A(II,J) = SUM
0041200 DO 3014 I = 2,NS,2
0041300 K = I / 2
0041400 AS(I,I-1) = - 39.47600 * PE(K) * PE(K)
0041500 AS(I-1,I) = 1.000
0041600 3014 AS(I,I) = - 12.56600 * ZE(K) * PE(K)
0041700 DO 3016 J = 1,NS
0041800 JJ = NP + J
0041900 DO 3016 I = 1,NS
0042000 II = NP + I
0042100 SUM = 0.000
0042200 DO 3015 K = 1,NSO
0042300 DO 3015 IL = 1,NSF

```

```

0042400 3015 SUM = SUM + ES(I,IL) * FS(IL,K) * CS(K,J)
0042500 3016 A(II,JJ) = AS(I,J) + SJM
0042500 C
0042700 C ADD EFFECT OF PRESSURE ON ACTUATOR POSITION FOR CONTROL AT 3
0042800 C
0042900 IF (IACT .NE. 3) GO TO 3025
0043000 DO 3022 I=25,N,2
0043100 3022 A(29,I) = A(29,I) + AP7 * AREAP * A(26,I)
0043200 3025 CONTINUE
0043300 DO 3018 J = 1,NC
0043400 DO 3018 I = 1,NS
0043500 II = NP + I
0043600 SUM = 0.000
0043700 DO 3017 K = 1,NSP
0043800 3017 SUM = SUM + ES(I,K) * PP(K,J)
0043900 3018 B(II,J) = SUM
0044000 HH(1,26) = 1.000
0044100 WRITE (6,PARIN)
0044200 2025 FORMAT (1X, 'FOR APPEP SEPARATION MODE, TYPE 1')
0044300 3019 FORMAT (1X, 'A = ')
0044400 4580 FORMAT (1X, 'ENTER ACTUATOR LOCATION ..10R20R3')
0044500 501 FORMAT (1X, 'DSP = ')
0044600 502 FORMAT (1X, 'FS = ')
0044700 503 FORMAT (1X, 'ES = ')
0044800 504 FORMAT (1X, 'DPS = ')
0044900 505 FORMAT (1X, 'B = ')
0045000 506 FORMAT (1X, 'D = ')
0045100 507 FORMAT (1X, 'AS = ')
0045200 508 FORMAT (1X, 'PP = ')
0045300 509 FORMAT (1X, 'CS = ')
0045400 510 FORMAT (1X, 'CP = ')
0045500 511 FORMAT (1X, 'C = ')
0045600 512 FORMAT (1X, 'HH = ')
0045700 C
0045800 C
0045900 C PRINT OUT THE A MATRIX
0046000 C
0046100 C
0046200 618 FORMAT(I2)
0046300 WRITE (6,3019)
0046400 CALL MATPRT (A, N, N, NMAX)
0046500 WRITE (6,505)
0046600 CALL MATPRT (B, N, NC, NMAX)
0046700 WRITE (6,506)
0046800 CALL MATPRT (D, N, ND, NMAX)
0046900 WRITE (6,511)
0047000 CALL MATPRT (C,NO,N,NOMAX)
0047100 WRITE (6,512)
0047200 CALL MATPRT (HH,NM,N,NMMAX)
0047300 IF (IAMAT .EQ. 0) GO TO 379
0047400 WRITE (3) ((A(I,J), J = 1,N), I = 1,N)
0047500 379 CONTINUE
0047520 C
0047540 C IF IDBUG .GT. 0, POGO SUBMATRICES ARE PRINTED OUT
0047560 C
0047600 IF (IDBUG) 39,39,38
0047700 38 WRITE (6,501)
0047800 CALL MATPRT (DSP, NSP, NPO, NSPMAX)
0047900 WRITE (6,502)
0048000 CALL MATPRT (FS, NSP, NSO, NSPMAX)
0048100 WRITE (6,503)
0048200 CALL MATPRT (ES, NS, NSP, NSMAX)
0048300 WRITE (6,504)
0048400 CALL MATPRT (DPS, NP, NSO, NPMAX)
0048500 WRITE (6,507)
0048600 CALL MATPRT (AS, NS, NS, NSMAX)
0048700 WRITE (6,508)
0048800 CALL MATPRT (PP, NSP, NC, NSPMAX)
0048900 WRITE (6,509)
0049000 CALL MATPRT (CS, NSO, NS, NSOMAX)
0049100 WRITE (6,510)
0049200 CALL MATPRT (CP, NPO, NP, NPOMAX)
0049300 39 CONTINUE
0049400 RETURN
0049500 END

```

## REFERENCES

1. Farrell, E. C.; and Fenwick, J. R.: Pogo Instabilities Suppression Evaluation (R-9125, Rockwell International Corp.; NASA Contract NAS3-14382.) NASA CR-134500, 1973.
2. Lock, M. H.; and Rubin, S.: Active Suppression of Pogo on the Space Shuttle. (ATR-75 (7428)-1; Aerospace Corp.; NASA Contract NAS3-17758.) NASA CR-134749, 1974.
3. Seidel, Robert C.; Lorenzo, Carl F.; and Lehtinen, Bruce: Space Shuttle Pogo Active Controller Design Using Frequency Domain Optimization. NASA TM X-3368, 1976.
4. Lock, M. N.; and Rubin, S.: Passive Suppression of Pogo on the Space Shuttle. (ATR-74(7416)-1; Aerospace Corp.; NASA Contract NAS1-12215.) NASA CR-132452, 1974.
5. Geysler, Lucille C.; and Lehtinen, Bruce: Digital Program for Solving the Linear Stochastic Optimal Control and Estimation Problem. NASA TN D-7820, 1975.
6. Kwatny, Harry G.; and Fink, Lester H.: Acoustics, Stability, and Compensation in Boiling Water Reactor Pressure Control Systems. IEEE Trans. Autom. Control, vol. AC-20, no. 3, Dec. 1975, pp. 727-739.
7. Shaw, Leonard: Pole Placement Stability and Sensitivity of Dynamic Compensators. IEEE Trans. Autom. Control, vol. AC-16, no. 2, Apr. 1971, p. 210.
8. Widnall, William S.: On the Design of Nearly Optimal Linear Time-Varying Sampled Data Stochastic Controllers. D.Sc. Thesis, MIT, 1966, pp. 89-103.
9. Hutton, M. F.; and Friedland, B.: Routh Approximations for Reducing Order of Linear Time-Invariant Systems. IEEE Trans. Autom. Control, vol. AC-20, no. 3, June 1975, pp. 329-337.

TABLE I. - PROPULSION SYSTEM PARAMETERS

First feedline cross-sectional area, $A_1$ , $\text{cm}^2$ ; $\text{in}^2$ . . . . .	487; 75.5
Second feedline cross-sectional area, $A_2$ , $\text{cm}^2$ ; $\text{in}^2$ . . . . .	487; 75.5
LPOP exit area, $A_3$ , $\text{cm}^2$ ; $\text{in}^2$ . . . . .	201; 31.2
HPOP suction area, $A_4$ , $\text{cm}^2$ ; $\text{in}^2$ . . . . .	83.3; 12.6
Effective thrust chamber area, $A_{tc}c_f$ , $\text{cm}^2$ ( $\text{in}^2$ ) . . . . .	1020; 158
Acoustic velocity, $a$ , $\text{m/sec}$ ; $\text{in/sec}$ . . . . .	5.183; 20 400
Lump compliance, $C_l$ , $\text{cm}^5/\text{N}$ ; $\text{in}^5/\text{lbf}$ . . . . .	5.94; 0.250
HPOP compliance, $C_{b1}$ , $\text{cm}^5/\text{N}$ ; $\text{in}^5/\text{lbf}$ . . . . .	5.94 - 23.8; 0.25 - 1
LPOP compliance, $C_{b2}$ , $\text{cm}^5/\text{N}$ ; $\text{in}^5/\text{lbf}$ . . . . .	2.38 - 2.98; 0.1 - 0.125
Mean flow of liquid oxygen, $\bar{I}$ , $\text{N}\cdot\text{sec}/\text{cm}$ ; $\text{lbf}\cdot\text{sec}/\text{in}$ . . . . .	4.01; 2.29
Gravitational constant, $g$ , $\text{cm}/\text{sec}^2$ ; $\text{in}/\text{sec}^2$ . . . . .	981.5; 386.4
Line lump length, $l$ , $\text{cm}$ ; $\text{in}$ . . . . .	345; 136
Lump inertance, $L_l$ , $\text{N}\cdot\text{sec}^2/\text{cm}^5$ ; $\text{lbf}\cdot\text{sec}^2/\text{in}^5$ . . . . .	$7.46 \times 10^{-6}$ ; $1.77 \times 10^{-4}$
Inner-pump duct inertance, $L_I$ , $\text{N}\cdot\text{sec}^2/\text{cm}^5$ ; $\text{lbf}\cdot\text{sec}^2/\text{in}^5$ . . . . .	$2.25 \times 10^{-5}$ ; $5.36 \times 10^{-4}$
LPOP inertance, $L_{p1}$ , $\text{N}\cdot\text{sec}^2/\text{cm}^5$ ; $\text{lbf}\cdot\text{sec}^2/\text{in}^5$ . . . . .	$1.73 \times 10^{-6}$ ; $4.12 \times 10^{-5}$
HPOP inertance, $L_{p2}$ , $\text{N}\cdot\text{sec}^2/\text{cm}^5$ ; $\text{lbf}\cdot\text{sec}^2/\text{in}^5$ . . . . .	$4.33 \times 10^{-6}$ ; $1.03 \times 10^{-4}$
Discharge line inertance, $L_d$ , $\text{N}\cdot\text{sec}^2/\text{cm}^5$ ; $\text{lbf}\cdot\text{sec}^2/\text{in}^5$ . . . . .	$2.60 \times 10^{-5}$ ; $6.18 \times 10^{-4}$
Injector inertance, $L_J$ , $\text{N}\cdot\text{sec}^2/\text{cm}^5$ ; $\text{lbf}\cdot\text{sec}^2/\text{in}^5$ . . . . .	$8.67 \times 10^{-6}$ ; $2.06 \times 10^{-4}$
LPOP gain, $m_1 + 1$ . . . . .	1.31 - 2.20
HPOP gain, $m_2 + 1$ . . . . .	1.42 - 1.54
Lump resistance, $R_l$ , $\text{N}\cdot\text{sec}/\text{cm}^5$ ; $\text{lbf}\cdot\text{sec}/\text{in}^5$ . . . . .	$4.14 \times 10^{-6}$ ; $9.85 \times 10^{-5}$
Inner-pump duct resistance, $R_I$ , $\text{N}\cdot\text{sec}/\text{cm}^5$ ; $\text{lbf}\cdot\text{sec}/\text{in}^5$ . . . . .	$1.91 \times 10^{-4}$ ; $4.53 \times 10^{-3}$
HPOP resistance, $R_{p2}$ , $\text{N}\cdot\text{sec}/\text{cm}^5$ ; $\text{lbf}\cdot\text{sec}/\text{in}^5$ . . . . .	$4.58 \times 10^{-3}$ ; 0.109
Discharge line resistance, $R_d$ , $\text{N}\cdot\text{sec}/\text{cm}^5$ ; $\text{lbf}\cdot\text{sec}/\text{in}^5$ . . . . .	$8.49 \times 10^{-4}$ ; $2.029 \times 10^{-2}$
Injector resistance, $R_J$ , $\text{N}\cdot\text{sec}/\text{cm}^5$ ; $\text{lbf}\cdot\text{sec}/\text{in}^5$ . . . . .	$6.17 \times 10^{-3}$ ; 0.147
Thrust chamber resistance, $R_c$ , $\text{N}\cdot\text{sec}/\text{cm}^5$ ; $\text{lbf}\cdot\text{sec}/\text{in}^5$ . . . . .	$4.33 \times 10^{-3}$ ; 0.103
Liquid-oxygen density, $\rho$ , $\text{g}/\text{cm}^3$ ; $\text{lb}/\text{in}^3$ . . . . .	1.055; $3.813 \times 10^{-2}$
Thrust chamber time constant, $\tau_c$ , $\text{sec}$ . . . . .	$4.5 \times 10^{-4}$
Actuator pole frequency, $\omega_a$ , $\text{rad}/\text{sec}$ . . . . .	100 $\pi$

TABLE II. - STRUCTURAL MODE DATA FOR END-BURN AND  
AFTER-SOLID-ROCKET-SEPARATION CONDITIONS

Parameter	End burn						After separation
	Mode						
	1	2	3	4	5	6	1
	Aerospace Corp. designation						
	E1	E2	E7	E30	E34	E35	A1
Modal displacement:							
$\varphi_i^{(x)}(\ell 1)$	-0.156	-0.198	0.054	0.022	0.222	0.022	0.529
$\varphi_i^{(x)}(1)$	-0.330	-0.245	-0.0787	-0.752	0.370	0.0134	0.208
$\varphi_i^{(x)}(3)$	-0.330	-0.245	-0.0787	-0.752	0.370	0.0134	0.208
$\varphi_i^{(x)}(4)$	0.255	0.239	-0.556	-1.71	-2.13	2.63	1.28
$\varphi_i^{(x)}(7)$	0.255	0.239	-0.556	-1.71	-2.13	2.63	1.28
$\varphi_i^{(x)}(tb)$	-0.209	-0.334	-0.259	-7.74	4.443	5.336	0.257
$\varphi_i^{(z)}(\ell 2)$	0.0367	-0.352	0.431	-0.372	0.017	-0.09	0.094
$\varphi_i^{(z)}(1)$	0.0367	-0.352	0.431	-0.372	0.017	-0.09	0.094
$\varphi_i^{(z)}(3)$	0.0367	-0.352	0.431	-0.372	0.017	-0.09	0.094
$\varphi_i^{(z)}(4)$	0.846	0.50	-1.95	-0.12	0.99	-1.56	1.68
$\varphi_i^{(z)}(7)$	0.846	0.50	-1.95	-0.12	0.99	-1.56	1.68
Modal pressure coefficient, $\varphi_i(tb)$ , N·sec <sup>2</sup> /cm <sup>3</sup>	0	0	0	0	0	0	$-2.16 \times 10^{-3}$
Generalized mass, $M_i$	292	292	292	292	292	292	1282
Damping, $\zeta_i$	0.01	0.01	0.01	0.01	0.01	0.01	0.01
Structural pole natural frequency, $\omega_i/2\pi$ , Hz	2.81	4.73	8.99	22.5	26.8	27.2	2.30

TABLE III. - NUMBER OF RIGHT-HALF-PLANE ZEROS

Control weighting, $r_2$	Ratio of normalized disturbance to measurement noise, $\tilde{\psi}_w/\tilde{\psi}_v$		
	1.95	19.5	195
	Number of right-half-plane zeros		
$2 \times 10^{-3}$	17	19	17
$2 \times 10^{-4}$	17	19	15
$2 \times 10^{-5}$	13	--	2
$4 \times 10^{-6}$	11	6	0

TABLE IV. - MODAL DAMPING RATIOS FOR MODAL CONTROL DESIGNS

[Weighting on modal state variable,  $\gamma_i$ , 1 for both critical modes; full-state feedback.]

(a) Open loop

Natural frequency, Hz	Damping ratio
100.00	0.7071
<sup>a</sup> 2.312	.3836 $\times 10^{-2}$
2.889	.1651
4.716	.9858 $\times 10^{-2}$
8.381	.4765 $\times 10^{-2}$
8.603	.6648 $\times 10^{-1}$
14.08	.4492 $\times 10^{-1}$
19.42	.4127 $\times 10^{-1}$
23.31	.1223
22.51	.8965 $\times 10^{-2}$
<sup>a</sup> 23.83	.1493 $\times 10^{-2}$
26.32	.1886 $\times 10^{-1}$
28.10	.1808 $\times 10^{-1}$
32.11	.1990 $\times 10^{-1}$
35.88	.1274 $\times 10^{-1}$
39.31	.7499 $\times 10^{-2}$
42.26	.4410 $\times 10^{-2}$
44.63	.2615 $\times 10^{-2}$
46.36	.1618 $\times 10^{-2}$
47.41	.1099 $\times 10^{-2}$
50.11	1.000
61.40	1.000
333.1	1.000

(b) Closed loop

Control weighting, $r_2$			
1.0		0.1	
Natural frequency, Hz	Damping ratio	Natural frequency, Hz	Damping ratio
<sup>a</sup> 2.315	0.4485 $\times 10^{-1}$	<sup>a</sup> 2.335	0.1386
2.889	.1651	2.889	.1651
4.716	.9858 $\times 10^{-2}$	4.716	.9858 $\times 10^{-2}$
8.381	.4765 $\times 10^{-2}$	8.381	.4765 $\times 10^{-2}$
8.603	.6648 $\times 10^{-1}$	8.608	.6648 $\times 10^{-1}$
14.08	.4492 $\times 10^{-1}$	14.08	.4492 $\times 10^{-1}$
<sup>a</sup> 23.84	.3673 $\times 10^{-1}$	<sup>a</sup> 23.99	.1152
22.51	.8965 $\times 10^{-2}$	19.42	.4127 $\times 10^{-1}$
19.42	.4127 $\times 10^{-1}$	22.51	.8965 $\times 10^{-2}$
23.31	.1223	23.31	.1223
26.32	.1886 $\times 10^{-1}$	26.32	.1886 $\times 10^{-1}$
28.10	.1808 $\times 10^{-1}$	28.10	.1863 $\times 10^{-1}$
32.11	.1990 $\times 10^{-1}$	32.11	.1990 $\times 10^{-1}$
35.88	.1274 $\times 10^{-1}$	35.89	.1274 $\times 10^{-1}$
39.31	.7499 $\times 10^{-2}$	39.31	.7499 $\times 10^{-2}$
42.26	.4410 $\times 10^{-2}$	42.26	.4410 $\times 10^{-2}$
44.63	.2615 $\times 10^{-2}$	44.53	.2615 $\times 10^{-2}$
46.36	.1618 $\times 10^{-2}$	46.36	.1618 $\times 10^{-2}$
47.41	.1099 $\times 10^{-2}$	47.41	.1099 $\times 10^{-2}$
50.11	1.000	50.11	1.000
61.40	1.000	61.40	1.000
100.00	.7071	100.00	.7071
333.1	1.000	333.1	1.000

<sup>a</sup>Critical mode.

TABLE V. - CONTROL GAINS FOR MODAL

CONTROL DESIGNS

State	State number	Control weighting, $r_2$	
		1.0	0.1
		Control gain	
Flow rate	1	0.0318	0.0871
	3	0.00152	0.00412
	5	-0.0289	-0.0793
	7	-0.0299	-0.0825
	9	-0.000572	-0.00224
	11	0.0303	0.0826
	13	0.0323	0.0886
	15	0.00333	0.00978
	17	-0.0281	-0.0767
	19	-0.0306	-0.0844
	21	-0.00215	-0.00681
	23	0.0298	-0.0813
	25	0.0603	0.174
	27	0.0168	0.0612
29	0.0406	0.125	
Pressure	2	2.14	6.76
	4	2.16	6.85
	6	0.0758	0.248
	8	-2.02	-6.37
	10	-2.00	-6.33
	12	0.134	0.414
	14	2.27	7.18
	16	2.30	7.28
	18	0.202	0.685
	20	-1.87	-5.91
	22	-1.87	-5.91
	24	0.235	0.729
	26	1.29	4.07
28	0.0448	0.157	
Displacement	30	1540	5200
	32	-33.6	-108
	34	89.3	292
	36	246	801
	38	1070	3410
	40	-14 600	-44 200
Velocity	31	216	677
	33	-1.27	-3.75
	35	4.09	12.1
	37	1.24	3.57
	39	3.04	8.47
	41	23.5	89.0

TABLE VI. - MATRICES  $A_s$ ,  $E_s$ ,  $C_s$ ,  $\bar{C}_s$ ,  $F_s$ , AND  $D_{sp}$

$$A_s = \left[ \begin{array}{cc|cc} 0 & 1 & & \\ \hline -(2\pi f_{n1})^2 - 4\pi \zeta_1 f_{n1} & & & 0 \\ \hline & 0 & 1 & \\ & \hline & & -(2\pi f_{n2})^2 - 4\pi \zeta_2 f_{n2} & \\ & 0 & & \hline & & & 0 & 1 \\ & & & \hline & & & & -(2\pi f_{n6})^2 - 4\pi \zeta_6 f_{n6} \end{array} \right]_{12 \times 12}$$

$$E_s = \left[ \begin{array}{cc|cc} 0 & & & \\ \hline 1/M_1 & & & 0 \\ \hline & 0 & 1 & \\ & \hline & & 1/M_2 & \\ & 0 & & \hline & & & 0 & 1/M_6 \end{array} \right]_{12 \times 6}$$

$$C_s = \left[ \begin{array}{c|c|c|c|c} \Phi_1 & \Phi_2 & \text{---} & \Phi_6 & \\ \hline 0 & 0 & \text{---} & 0 & \end{array} \right]_{12 \times 6}$$

$$\bar{C}_s = \left[ \begin{array}{c|c|c|c|c|c} 0 & 0 & 0 & 0 & & 0 \\ \hline 0 & 0 & 0 & 0 & & 0 \\ \hline 0 & \mathcal{P}_1(tb) & 0 & \mathcal{P}_2(tb) & \text{---} & \mathcal{P}_6(tb) \end{array} \right]_{12 \times 12}$$

TABLE VI. - Continued.

$(F_s)_{6 \times 12}$   $i = 1, 2, \dots, 6:$

$$(F_s)_{i,1} = -A_1^2 R_\ell \varphi_i^{(x)}(\ell 1)$$

$$(F_s)_{i,2} = -\bar{f} \varphi_i^{(x)}(1)$$

$$(F_s)_{i,3} = \bar{f} \varphi_i^{(x)}(3) + 2\bar{f} \varphi_i^{(z)}(3)$$

$$(F_s)_{i,4} = -\bar{f} \varphi_i^{(x)}(4)$$

$$(F_s)_{i,5} = (F_s)_{i,6} = 0$$

$$(F_s)_{i,7} = -A_2^2 R_\ell \varphi_i^{(z)}(\ell 2)$$

$$(F_s)_{i,8} = \bar{f} \varphi_i^{(z)}(1)$$

$$(F_s)_{i,9} = \bar{f} \varphi_i^{(z)}(3)$$

$$(F_s)_{i,10} = \bar{f} \varphi_i^{(z)}(4) - \frac{R_{p1} A_3^2 L_I}{L_I + L_{p1}} \varphi_i^{(z)}(4)$$

$$(F_s)_{i,11} = \left\{ -A_3^2 R_3 - A_4^2 \left[ R_4 + R_{p2} - \left( \frac{R_d + R_j + R_{p2}}{L_d + L_j + L_{p2}} \right) (L_j + L_{p2}) + R_j \right] \right\} \varphi_i^{(z)}(7) + \frac{L_{p1}}{L_I + L_{p1}} R_1 A_3^2 \varphi_i^{(z)}(4)$$

$$(F_s)_{i,12} = 0$$

$(D_{sp})_{6 \times 29}$   $i = 1, 2, \dots, 6:$

$$(D_{sp})_{i,2} = \frac{-\mathcal{P}_i^{(tb)}}{L_\ell}$$

$$(D_{sp})_{i,j} = 0 \quad j = 4, 6, 8, 10, 12, 14, 16, 20, \text{ and } 22$$

$$(D_{sp})_{i,j} = -A_1 R_\ell \varphi_i^{(x)}(\ell 1) - \frac{\mathcal{P}_i^{(tb)} R_\ell}{L_\ell}$$

$$(D_{sp})_{i,j} = -A_1 R_\ell \varphi_i^{(x)}(\ell 1) \quad j = 3, 5, 7, 9, 11, 13, \text{ and } 15$$

$$(D_{sp})_{i,17} = -A_1 R_\ell \varphi_i^{(x)}(\ell 1) - \frac{2\bar{f}}{A_1} \varphi_i^{(x)}(1)$$

TABLE VI. - Concluded.

$$(D_{sp})_{i,18} = -A_1 \varphi_i^{(x)}(1) - A_2 \varphi_i^{(z)}(1)$$

$$(D_{sp})_{i,19} = A_2 R_l \varphi_i^{(z)}(l, 2) - \frac{2\bar{f}}{A_2} \varphi_i^{(z)}(1)$$

$$(D_{sp})_{i,21} = A_2 R_l \varphi_i^{(z)}(l, 2)$$

$$(D_{sp})_{i,23} = A_2 R_l \varphi_i^{(z)}(l, 2) + \frac{2\bar{f}}{A_2} [\varphi_i^{(x)}(3) - \varphi_i^{(x)}(4) + \varphi_i^{(z)}(3)]$$

$$(D_{sp})_{i,24} = A_2 [\varphi_i^{(x)}(3) + \varphi_i^{(z)}(3) + \varphi_i^{(x)}(4)] - \frac{(m_1 + 1)L_1}{L_1 + L_{p1}} A_3 \varphi_i^{(z)}(4)$$

$$(D_{sp})_{i,25} = \frac{2\bar{f}}{A_3} [\varphi_i^{(z)}(7) - \varphi_i^{(z)}(4)] + A_3 R_3 \varphi_i^{(z)}(7) - \left( \frac{R_1 L_{p1} - R_{p1} L_1}{L_1 + L_{p1}} \right) A_3 \varphi_i^{(z)}(4)$$

$$(D_{sp})_{i,26} = - \left( \frac{L_{p1}}{L_1 + L_{p1}} \right) A_3 \varphi_i^{(z)}(4) + \left[ \frac{A_4(m_2 + 1)L_j}{L_d + L_j + L_{p2}} + A_3 - A_4(m_2 + 1) \left( \frac{L_d + L_j}{L_d + L_j + L_{p2}} \right) \right] \varphi_i^{(z)}(7)$$

$$(D_{sp})_{i,27} = A_4 \left[ \left( \frac{R_{p2} L_d - 2L_j R_d + R_j L_{p2}}{L_d + L_j + L_{p2}} \right) + R_4 - \frac{2\bar{f}}{A_4} \right] \varphi_i^{(z)}(7)$$

$$(D_{sp})_{i,28} = A_4 \left( \frac{L_d}{L_d + L_j + L_{p2}} \right) \varphi_i^{(z)}(7) + A_{tc} c_f \varphi_i^{(x)}(7)$$

$$(D_{sp})_{i,29} = 0$$

$$(F_q)_{6 \times 12} = \begin{bmatrix} 0 & (f_q)_{1,1} & 0 & & & (f_q)_{1,6} \\ & (f_q)_{2,1} & & & & (f_q)_{2,6} \\ & \vdots & & & & \vdots \\ & (f_q)_{6,1} & 0 & & & (f_q)_{6,6} \end{bmatrix}$$

where

$$(f_q)_{i,j} \triangleq A_1 \left[ \mathcal{P}_j^{(tb)} \varphi_i^{(x)}(tb) + \mathcal{P}_i^{(tb)} \varphi_j^{(x)}(tb) \right] + \frac{\mathcal{P}_i^{(tb)} \mathcal{P}_j^{(tb)}}{L_l}$$

TABLE VII. - MATRICES  $A_{p'}$ ,  $B_{p'}$ ,  $D_{p'}$ , AND  $D_{ps}$

	1	2	3	4	...	17	18	19	...	23	24	25	26	27	28	29	
1	$-\frac{R_1}{L_1}$	$-\frac{1}{L_1}$															
2	$\frac{1}{C_1}$	0	$-\frac{1}{C_1}$														
3		$\frac{1}{L_2}$	$-\frac{R_2}{L_2}$	$-\frac{1}{L_2}$													
4			$\frac{1}{C_1}$	0													
...																	
17						$\frac{1}{L_2}$	$-\frac{R_2}{L_2}$	$-\frac{1}{L_2}$									
18						$\frac{1}{C_1}$	0	$-\frac{1}{C_1}$									
19							$\frac{1}{L_2}$	$-\frac{R_2}{L_2}$									
...																	
23										$\frac{1}{L_2}$	$-\frac{R_2}{C_1}$	$-\frac{1}{L_2}$					
24										$\frac{1}{C_{b1}}$	0	$-\frac{1}{C_{b1}}$					
25											$\frac{m_1+1}{L_1+L_{p1}}$	$-\frac{R_1+R_{p1}}{L_1+L_{p1}}$	$-\frac{1}{L_1+L_{p1}}$				
26											$\frac{1}{C_{b2}}$	0	$-\frac{1}{C_{b2}}$	0	0	$\frac{1}{C_{b2}}$	
27												$\frac{m_2+1}{L_d+L_j+L_{p2}}$	$-\frac{R_d+R_j+R_{p2}}{L_d+L_j+L_{p2}}$	$-\frac{1}{L_d+L_j+L_{p2}}$			
28													$\frac{R_c}{r_c}$	$-\frac{1}{r_c}$			
29																	$-\omega_a$

$(A_{p'})_{29 \times 29}$

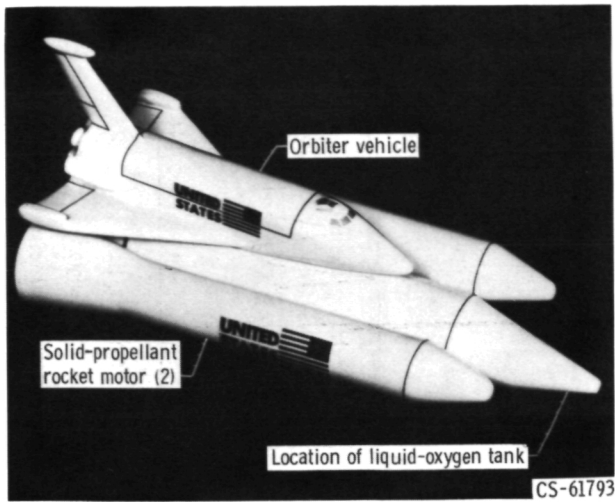
TABLE VII. - Concluded.

$$B_p = \begin{bmatrix} 0 \\ 0 \\ \vdots \\ \omega_a \end{bmatrix}_{29 \times 1}$$

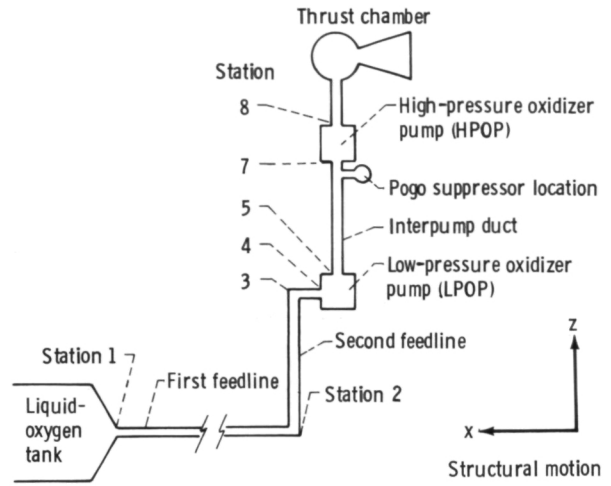
$$D_p = \begin{bmatrix} 0 \\ 0 \\ \vdots \\ \frac{1}{C_{b2}} \\ 0 \\ 0 \\ 0 \end{bmatrix}_{29 \times 1}$$

$(D_{p2})_{29 \times 12} =$

	1	2	3	4	5	6	7	8	9	10	11	12
1	$-R_1 A/L_1$											$L/L_1$
2	0											
3	$-R_1 A/L_1$											
4	0											
5	$-R_1 A/L_1$											
6	0											
7	$-R_1 A/L_1$											
8	0											
9	$-R_1 A/L_1$											
10	0											
11	$-R_1 A/L_1$											
12	0											
13	$-R_1 A/L_1$											
14	0											
15	$-R_1 A/L_1$											
16	0											
17	$-R_1 A/L_1$											
18		$A/C_1$						$A/C_1$				
19							$R_1 A/L_1$					
20												
21							$R_1 A/L_1$					
22												
23							$R_1 A/L_1$					
24			$-A/C_{b1}$	$A/C_{b1}$					$-A/C_{b1}$	$A_3/C_{b1}$		
25										$R_{p1} A_3^{a5}$	$R_1 A_3^{a5}$	
26											$(A_4 - A_3)/C_{b2}$	
27											$A_4^{a6}$	
28											$-R_c A_4 / \tau_c$	
29												



(a) Overall geometry.



(b) Schematic of liquid-oxygen system.

Figure 1. - Space shuttle system for pogo analysis.

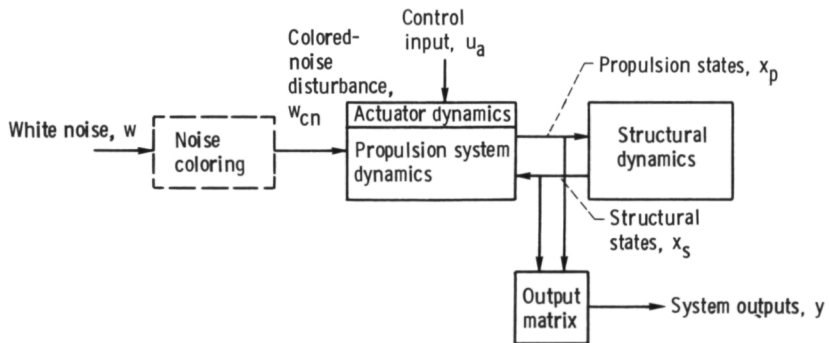


Figure 2. - State-variable model for pogo analysis.

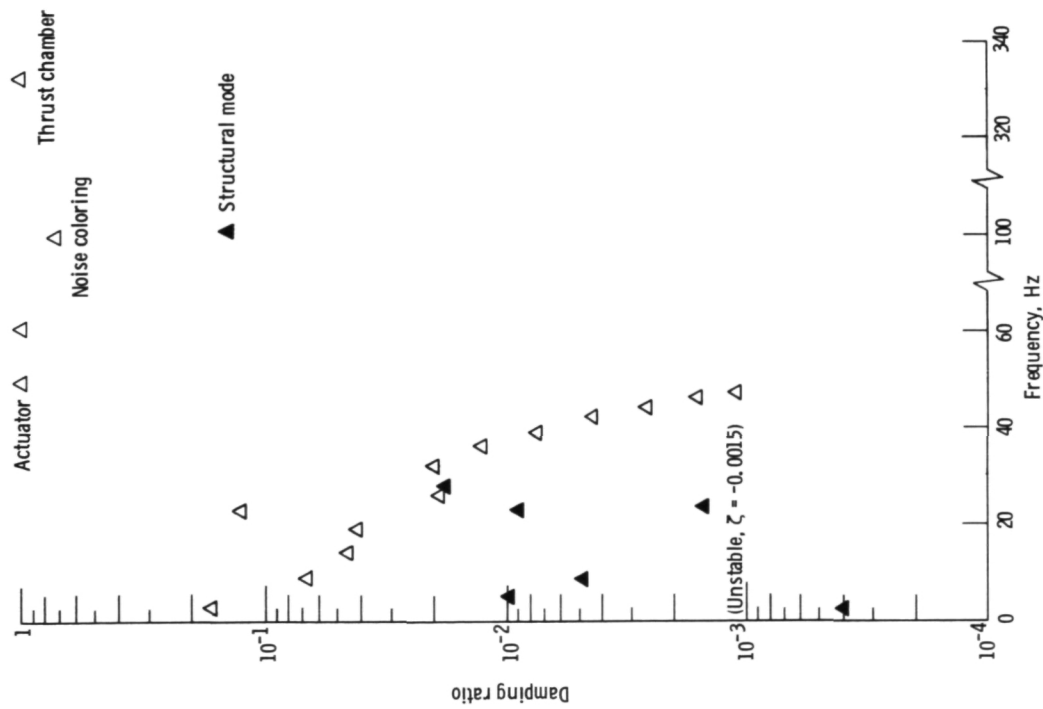


Figure 3. - Open-loop eigenvalues of overall coupled structure - propulsion system, worst-case model.

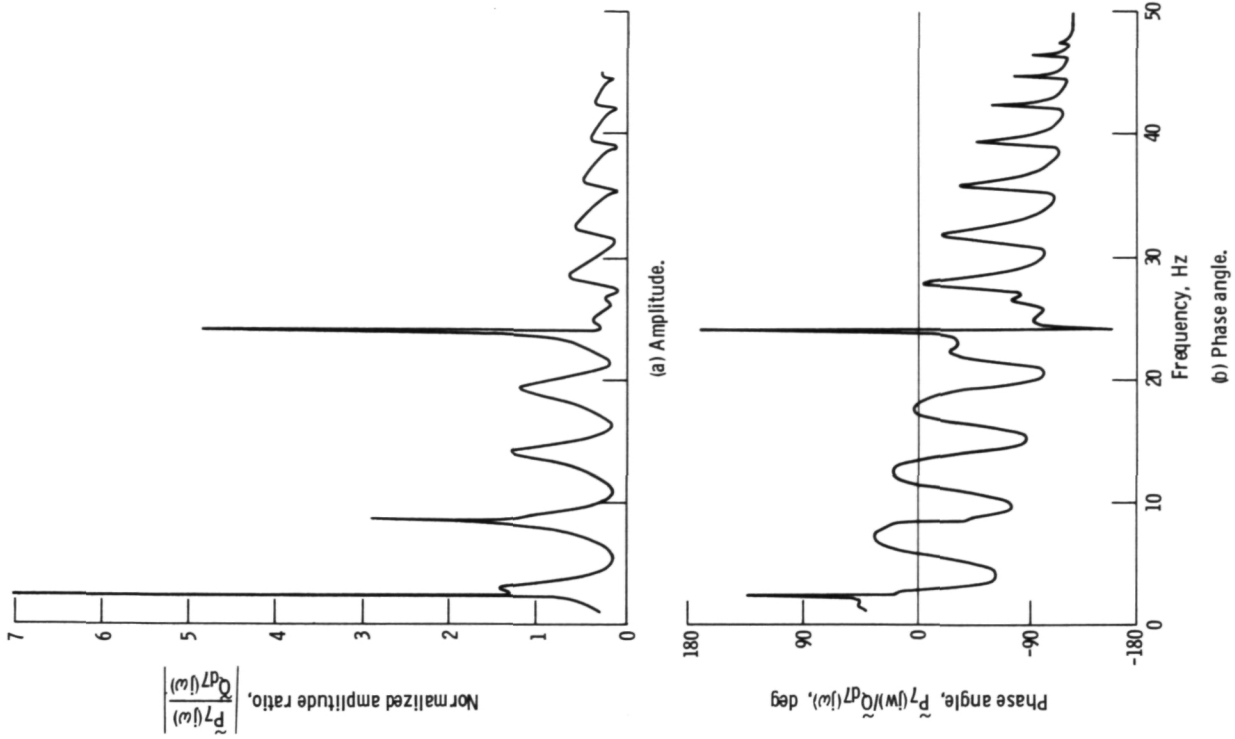


Figure 4. - Open-loop frequency response of overall coupled structure - propulsion system, worst-case model ( $P_7$  response to  $Q_{47}$ ).

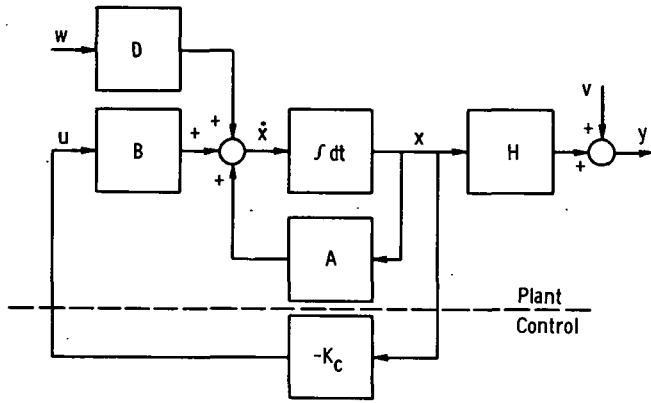


Figure 5. - Linear quadratic regulator solution for full-state feedback.

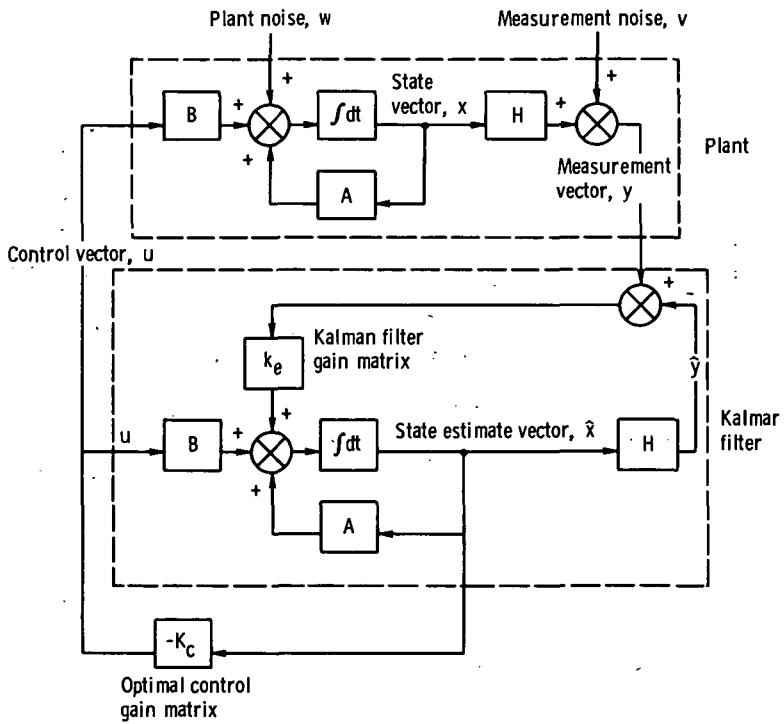


Figure 6. - Linear quadratic regulator solution with Kalman filter in feedback loop.

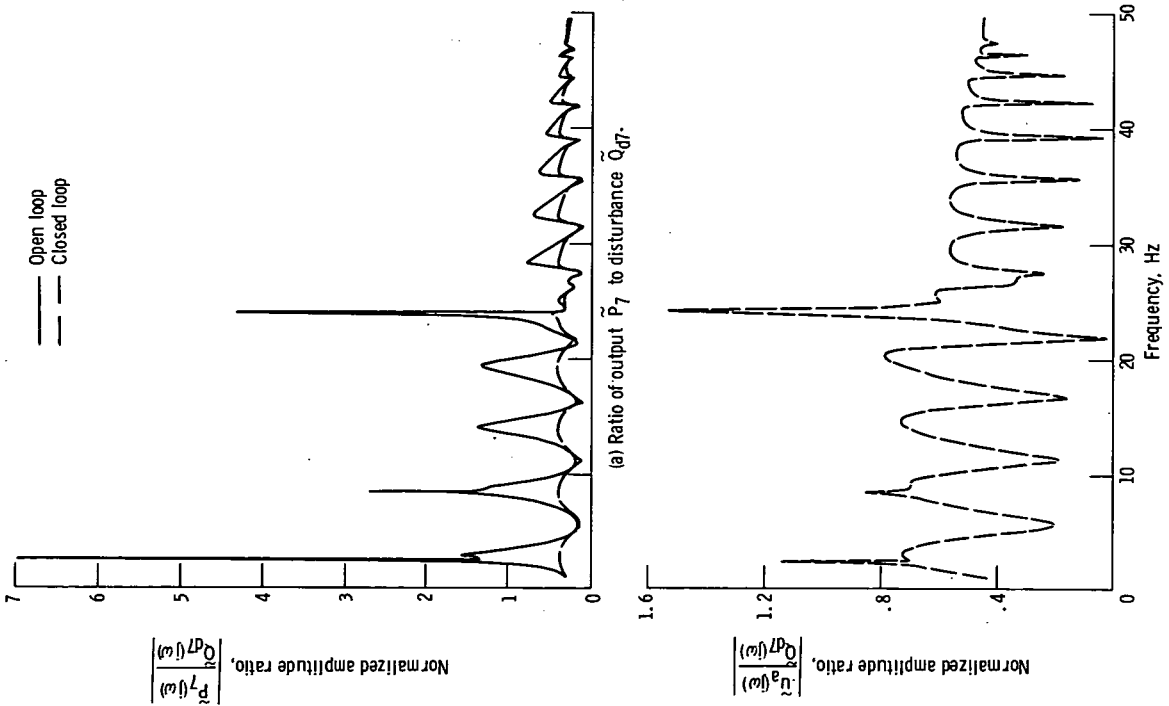


Figure 7. - Normalized frequency-response amplitude ratios. Full-state feedback; minimum-rms design; control weighting,  $r_2$  0.002.

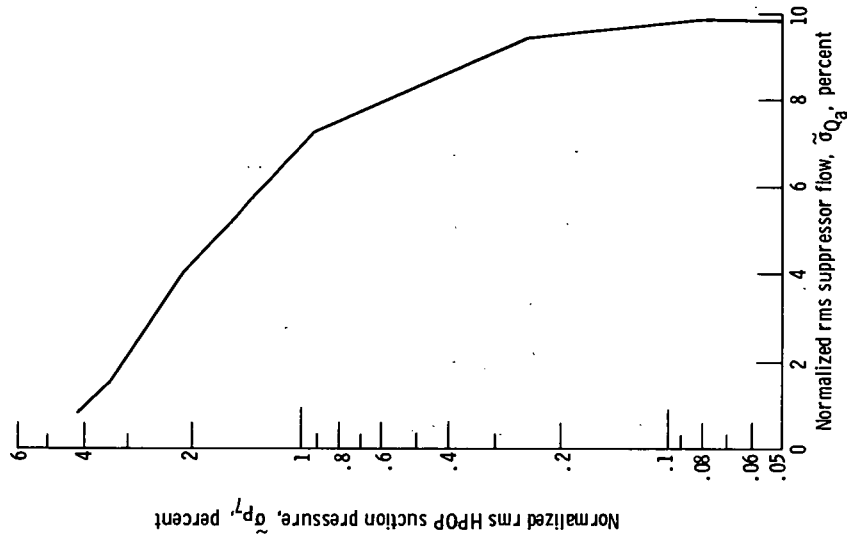


Figure 8. - Normalized root-mean-square high-pressure-oxidizer-pump pressure as function of normalized rms suppressor flow - full-state feedback. Minimum-rms design; rms value of disturbance  $\tilde{Q}_{d7}$ , 10 percent.

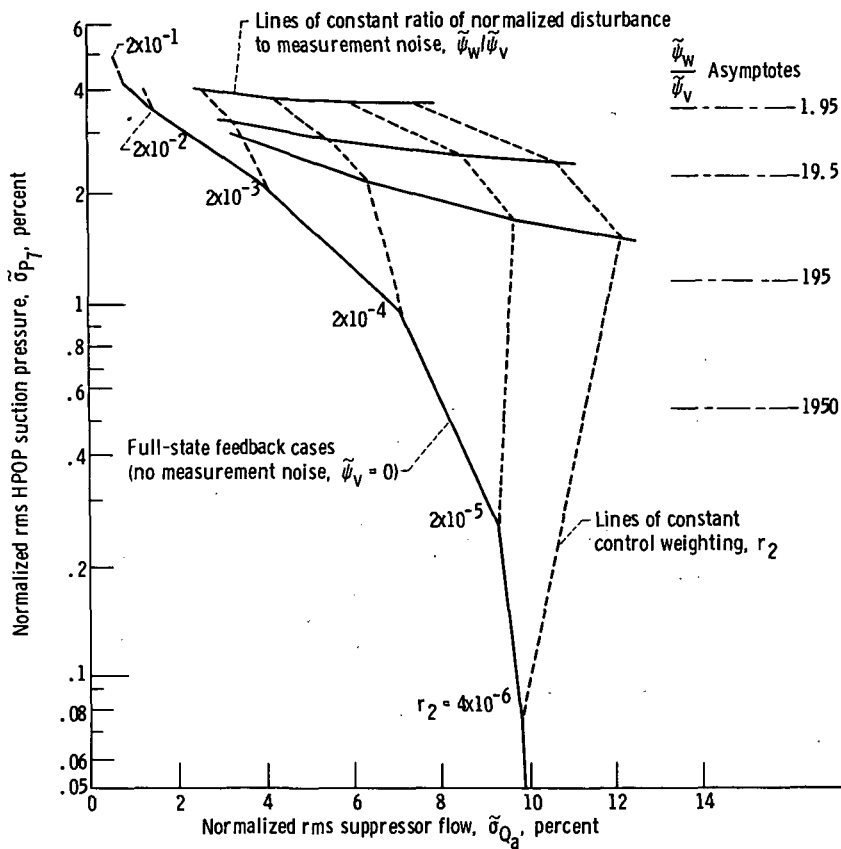


Figure 9. - Normalized root-mean-square high-pressure-oxidizer-pump suction pressure as function of normalized rms suppressor flow - Kalman filter on measurement  $P_{7m}$ . Minimum-rms design; rms value of disturbance  $Q_{d7}$ , 10 percent.

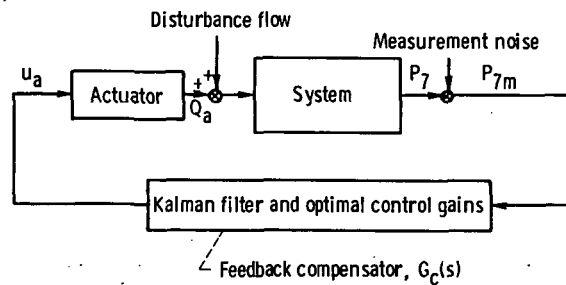


Figure 10. - System configuration showing Kalman filter and optimal control gains as feedback compensator.

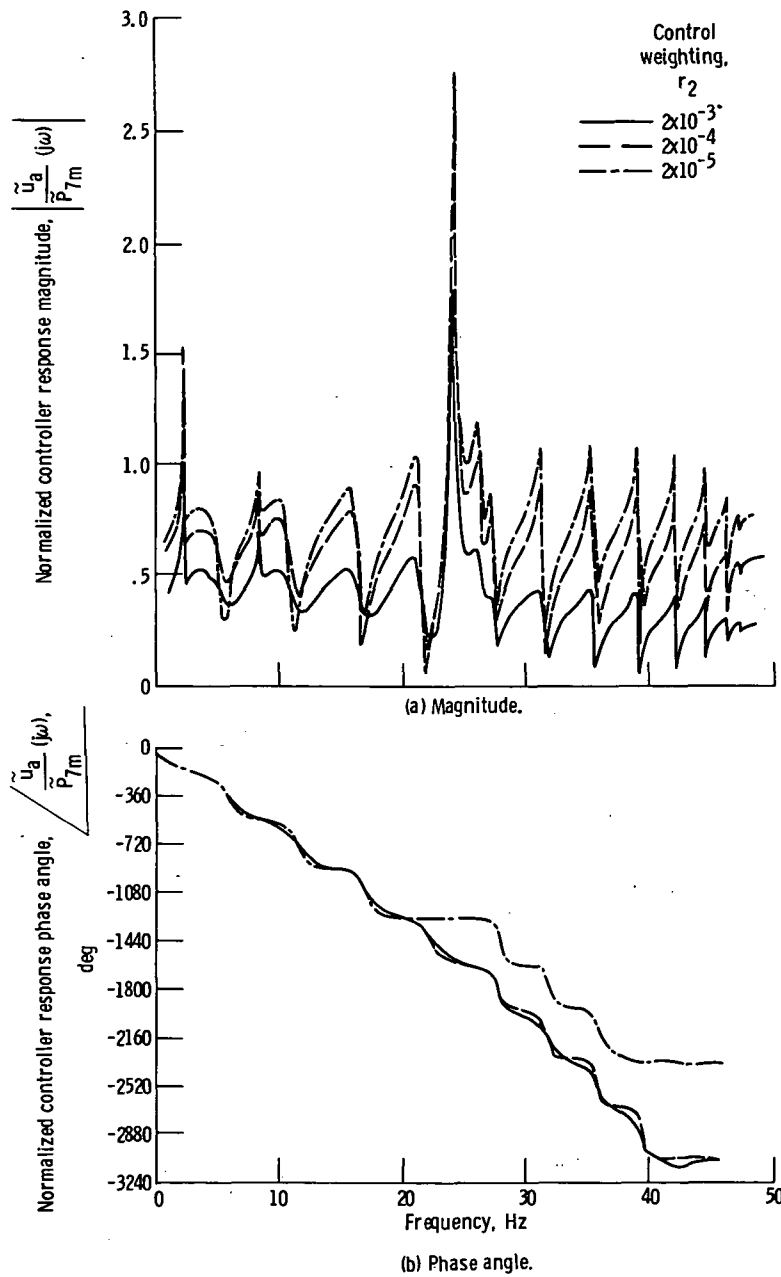
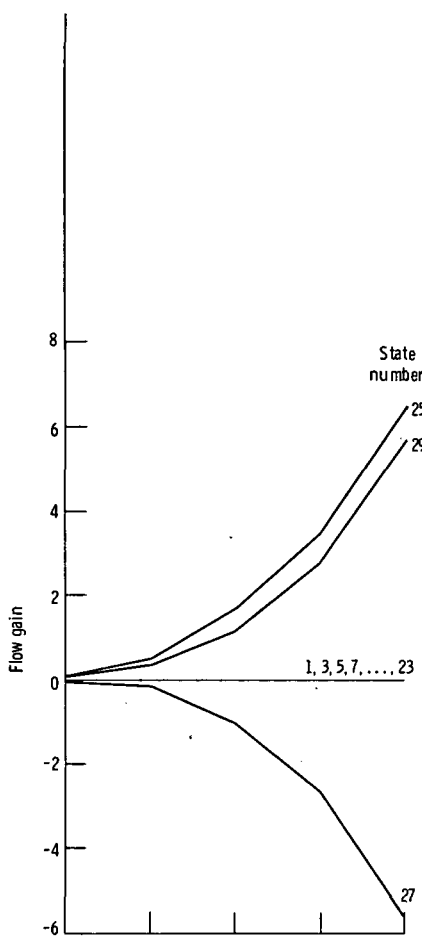
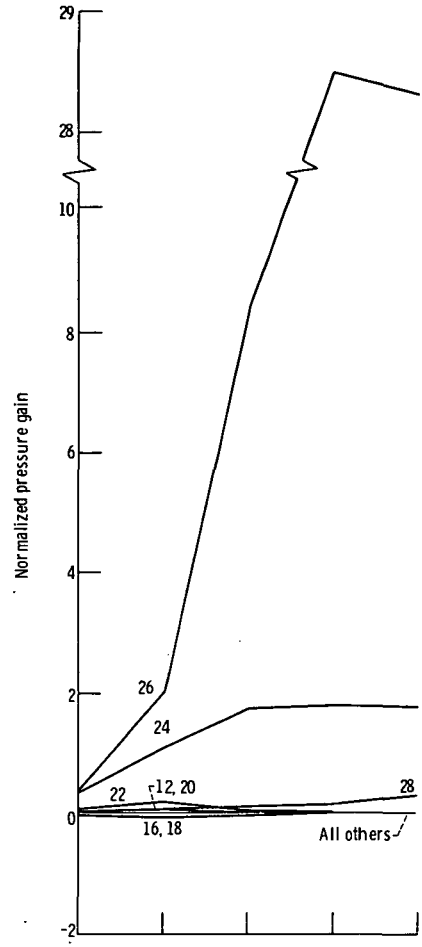


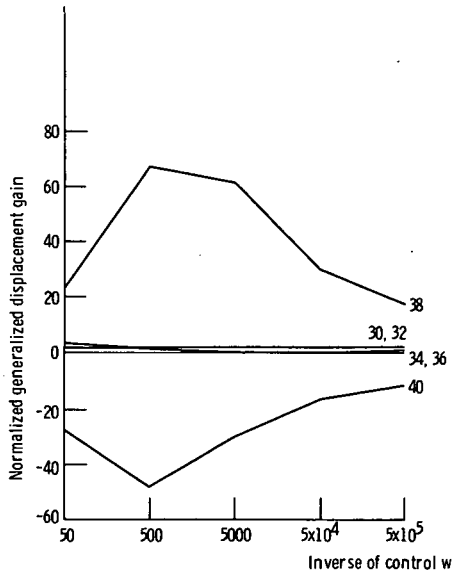
Figure 11. - Frequency response of feedback-compensator transfer function for different control gain sets. Kalman filter gains for ratio of disturbance to measurement noise  $\tilde{\psi}_w/\tilde{\psi}_v$  of 1.95.



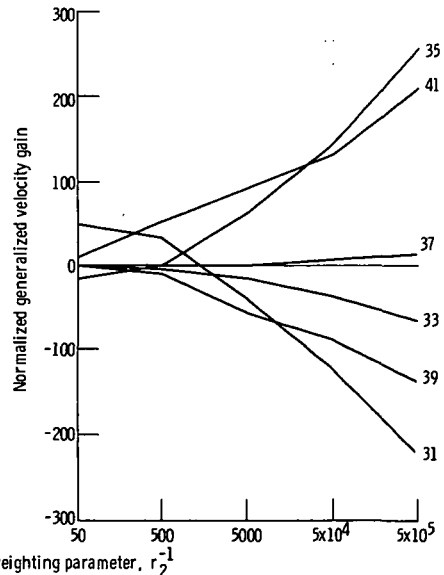
(a) Flow feedback gains.



(b) Pressure feedback gains.



(c) Generalized displacement feedback gains.



(d) Generalized velocity feedback gains.

Figure 12. - Linear quadratic regulator feedback gains as function of inverse control weighting. Minimum-rms control designs.

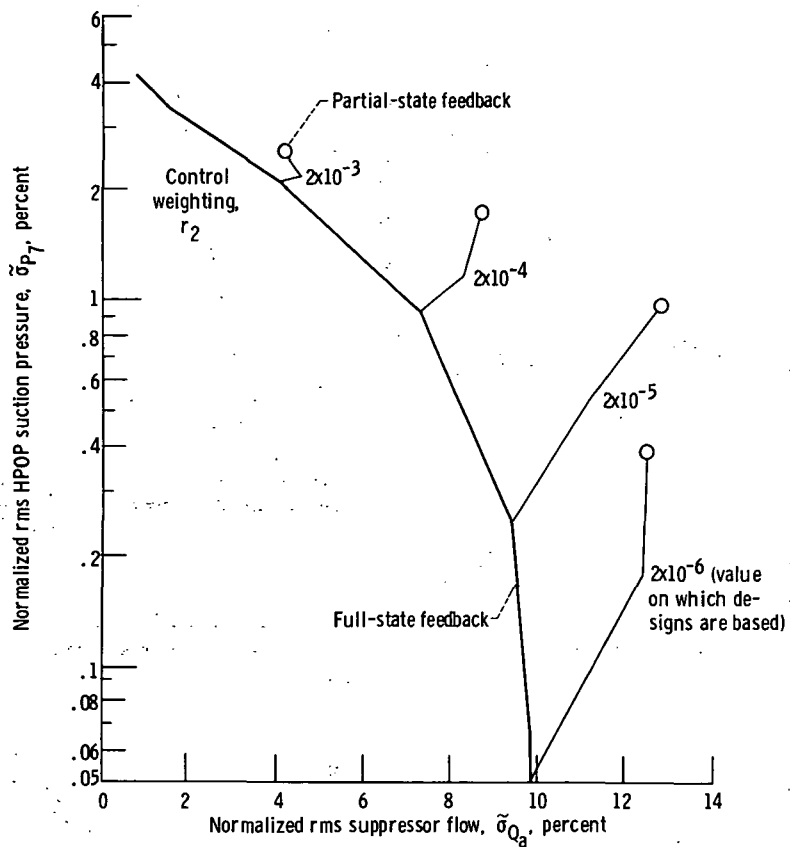


Figure 13. - Normalized root-mean-square high-pressure-oxidizer-pump suction pressure as function of normalized rms suppressor flow - partial-state feedback designs compared with full-state feedback designs. Minimum-rms design; no measurement noise; rms value of disturbance  $Q_{d7}$ , 10 percent.

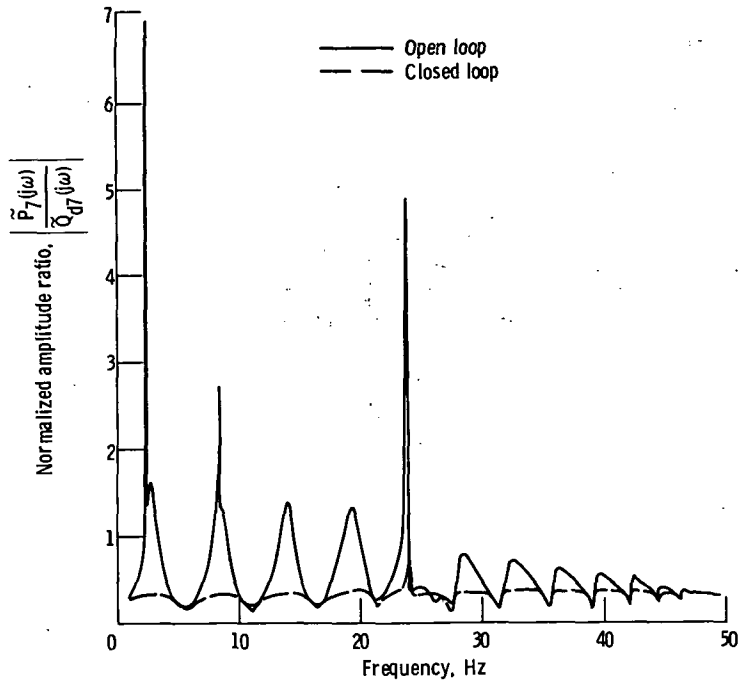


Figure 14. - Normalized frequency-response amplitude ratio of output  $\tilde{P}_7$  to disturbance  $\tilde{Q}_{d7}$  - minimum-rms, partial-state feedback design where control weighting  $r_2$  is  $2 \times 10^{-3}$ .

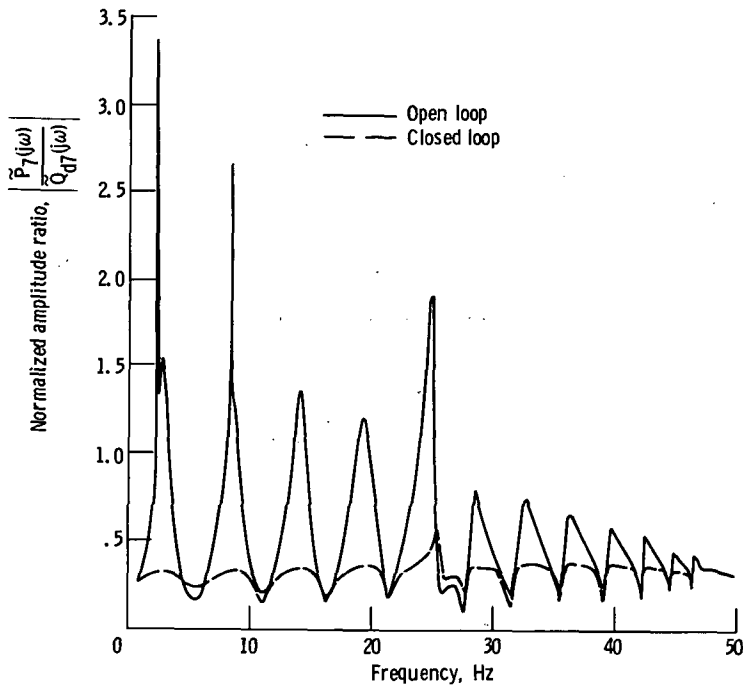


Figure 15. - Normalized frequency-response amplitude ratio of output  $\tilde{P}_7$  to disturbance  $\tilde{Q}_{d7}$  - where 23.8-hertz modal frequency has been increased by 10 percent. Minimum-rms, partial-state feedback design based on full-state feedback design where control weighting  $r_2$  is  $2 \times 10^{-3}$ .

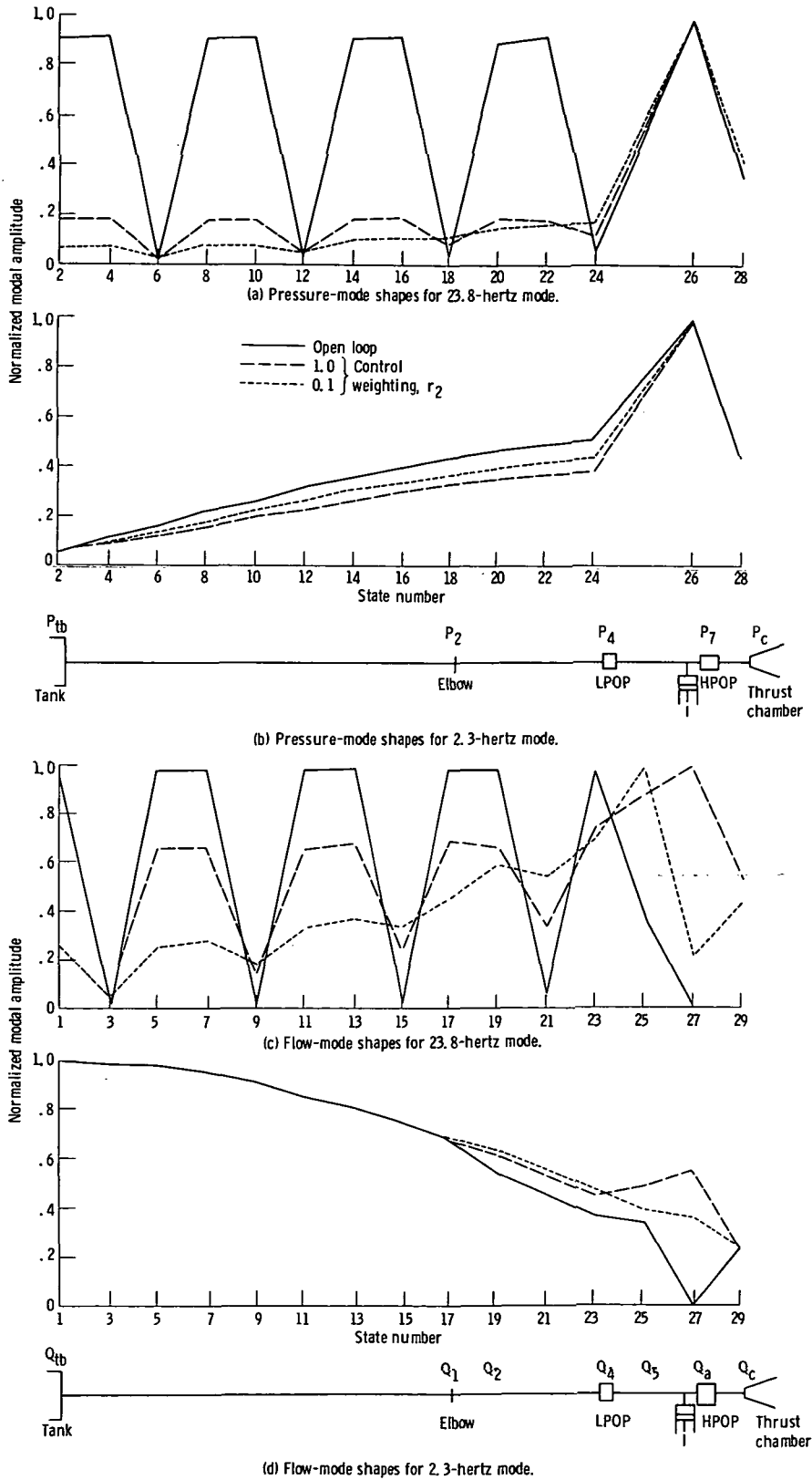
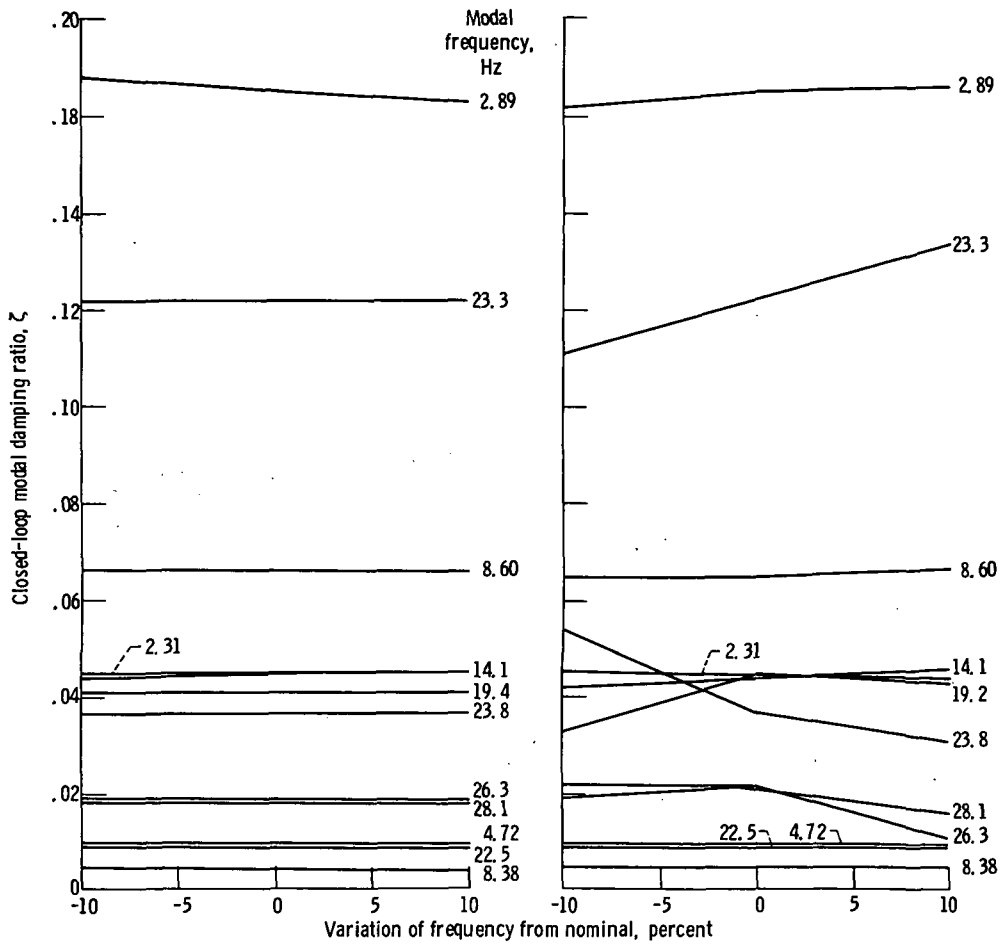


Figure 16. - Open- and closed-loop mode shapes for full-state feedback - modal control design.



(a) Critical structural mode, 2.3 hertz.

(b) Critical structural mode, 23.8 hertz.

Figure 17. - Sensitivity of closed-loop modal damping ratios to critical structural mode frequency - full-state feedback. Gains used from design for control weighting  $r_2$  of 1.0.

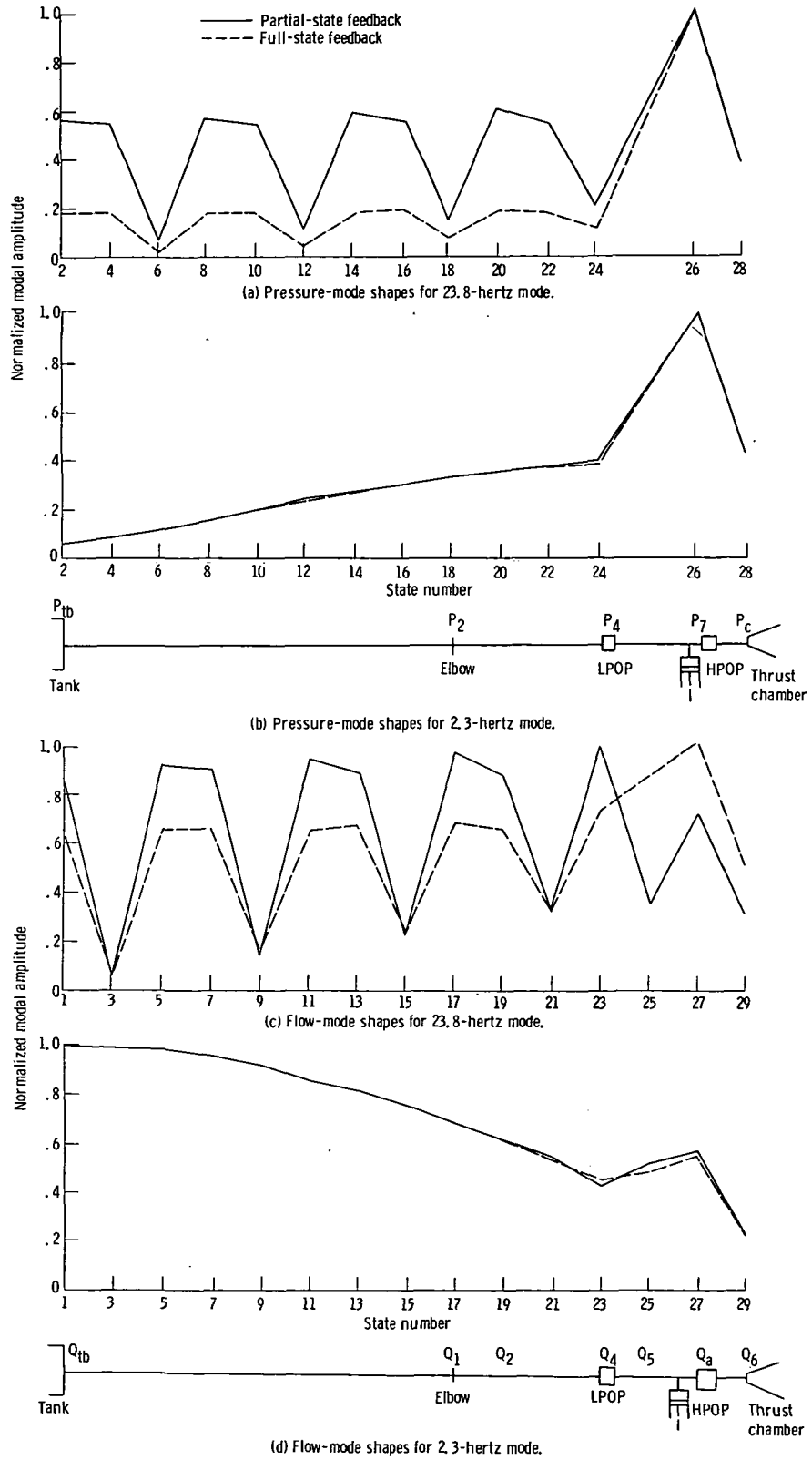


Figure 18. - Mode shapes for full- and partial-state feedback - modal control designs based on control weighting  $r_2$  of 1.0.

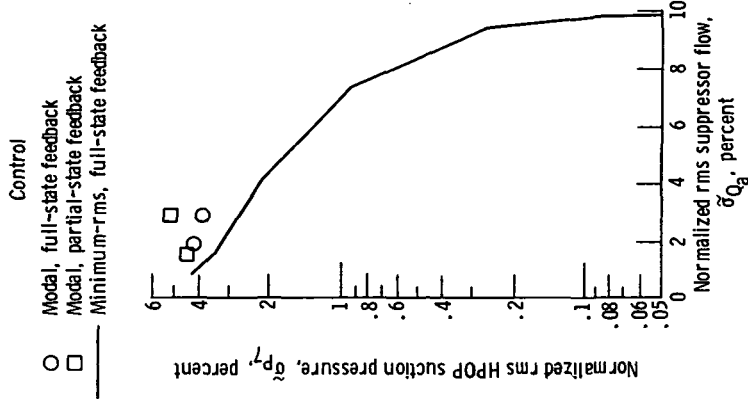
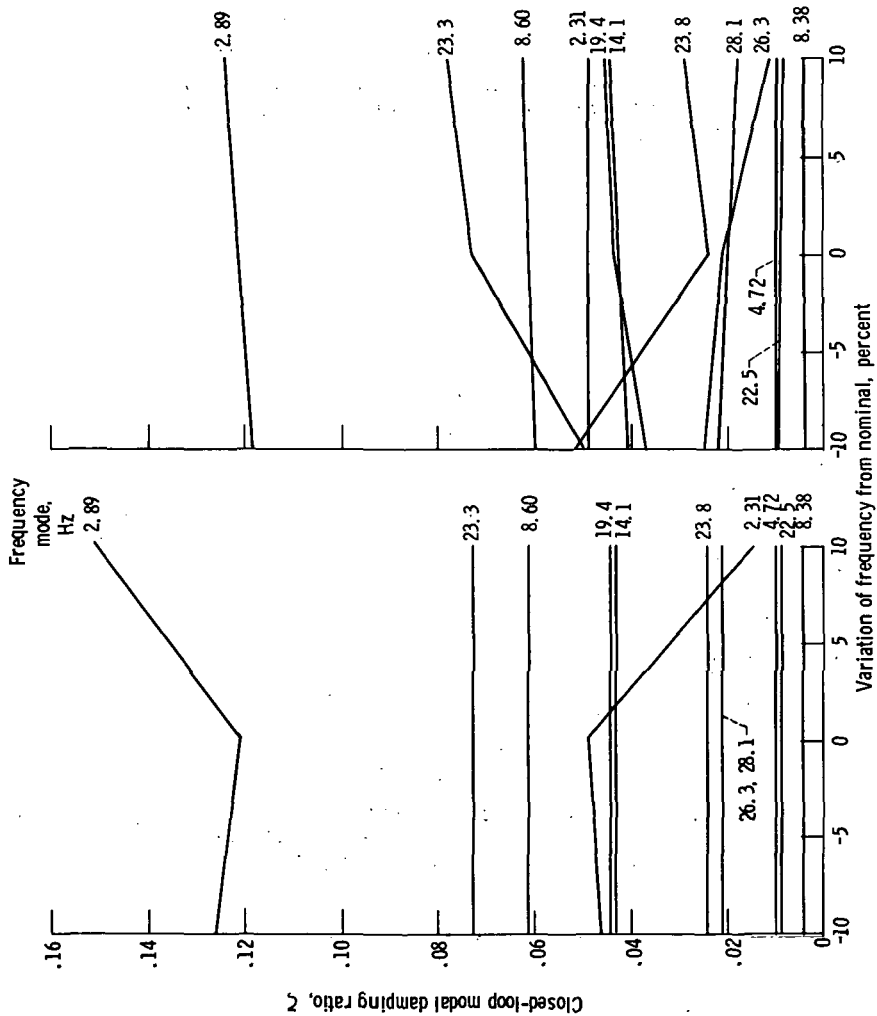


Figure 20. - Normalized root-mean-square high-pressure-oxidizer-pump pressure as function of normalized rms suppressor flow - modal control, full- and partial-state feedback designs compared with minimum-rms, full-state feedback designs. Root-mean-square value of disturbance  $\bar{Q}_{Q_1}$ , 10 percent.



(a) Critical structural mode, 2.3 hertz.  
 (b) Critical structural mode, 23.8 hertz.  
 Figure 19. - Sensitivity of closed-loop modal damping ratios to critical structural mode frequency - partial-state feedback design based on full-state feedback design for control weighting  $r_2$  of 1.0.

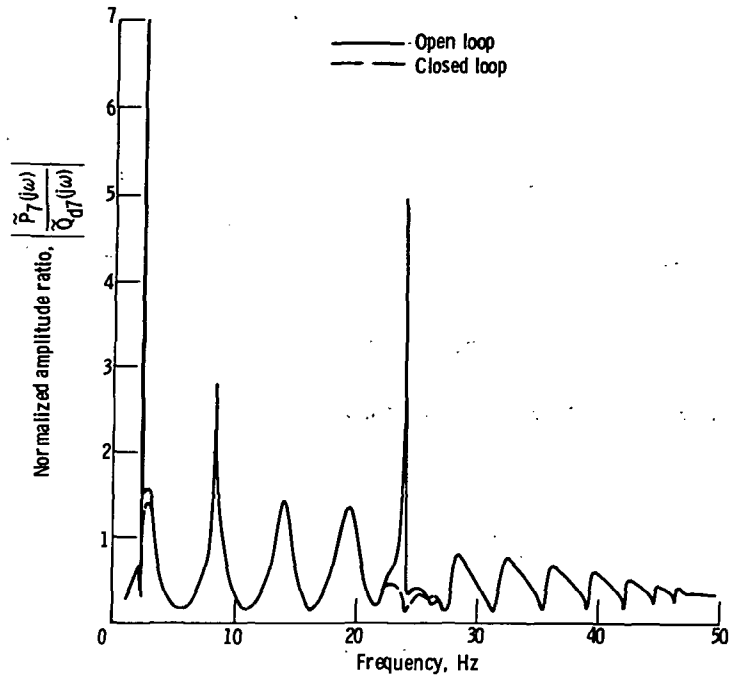


Figure 21. - Normalized frequency-response amplitude ratio of output  $\tilde{P}_7$  to disturbance  $\tilde{Q}_{d7}$  - modal control, full-state feedback design. Control weighting,  $r_2$  1.0.

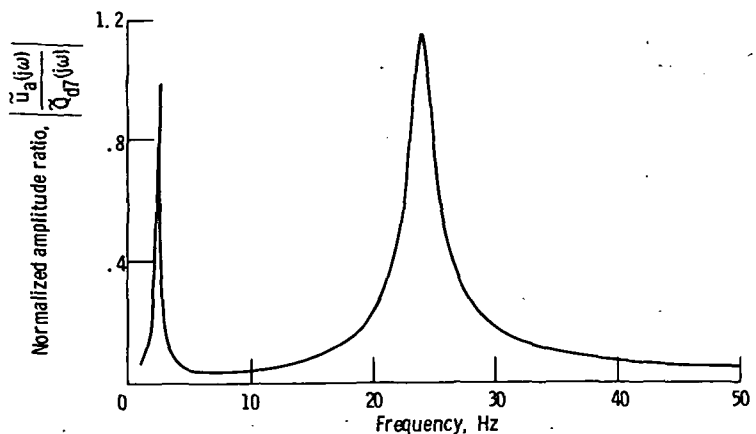


Figure 22. - Normalized, closed-loop frequency-response amplitude ratio of control input  $\tilde{u}_a$  to disturbance  $\tilde{Q}_{d7}$  - modal control, full-state feedback design. Control weighting,  $r_2$  1.0.

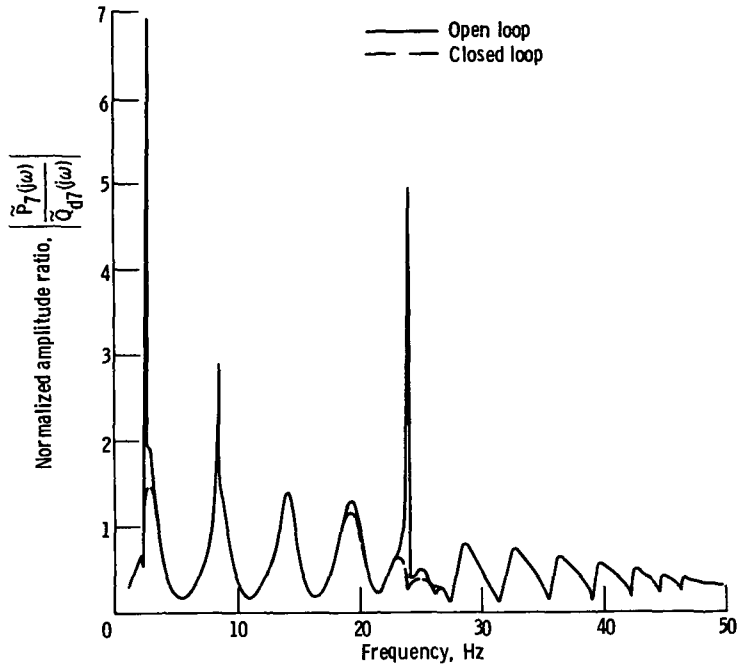


Figure 23. - Normalized frequency-response amplitude ratio of output  $\tilde{P}_7$  to disturbance  $\tilde{Q}_{d7}$  - modal control, partial-state feedback design based on full-state feedback design for control weighting  $r_2$  of 1.0.

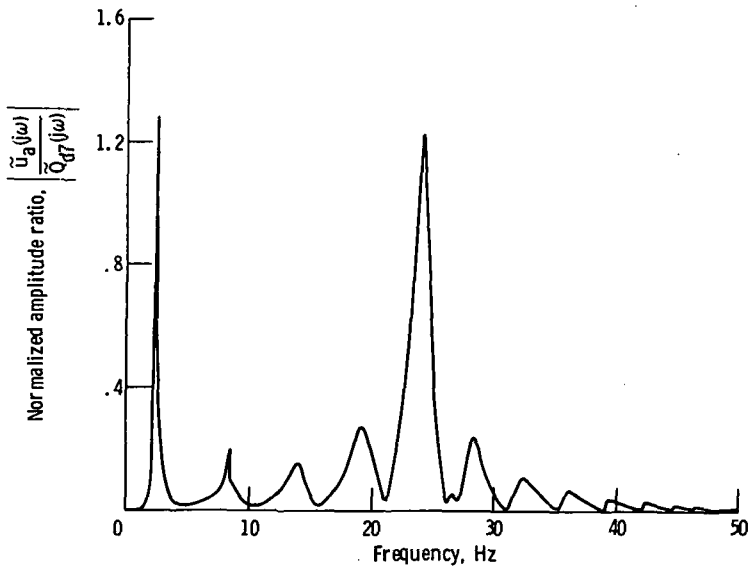


Figure 24. - Normalized, closed-loop frequency-response amplitude ratio of control input  $\tilde{U}_a$  to disturbance  $\tilde{Q}_{d7}$  - modal control, partial-state feedback design based on full-state feedback design for control weighting  $r_2$  of 1.0.

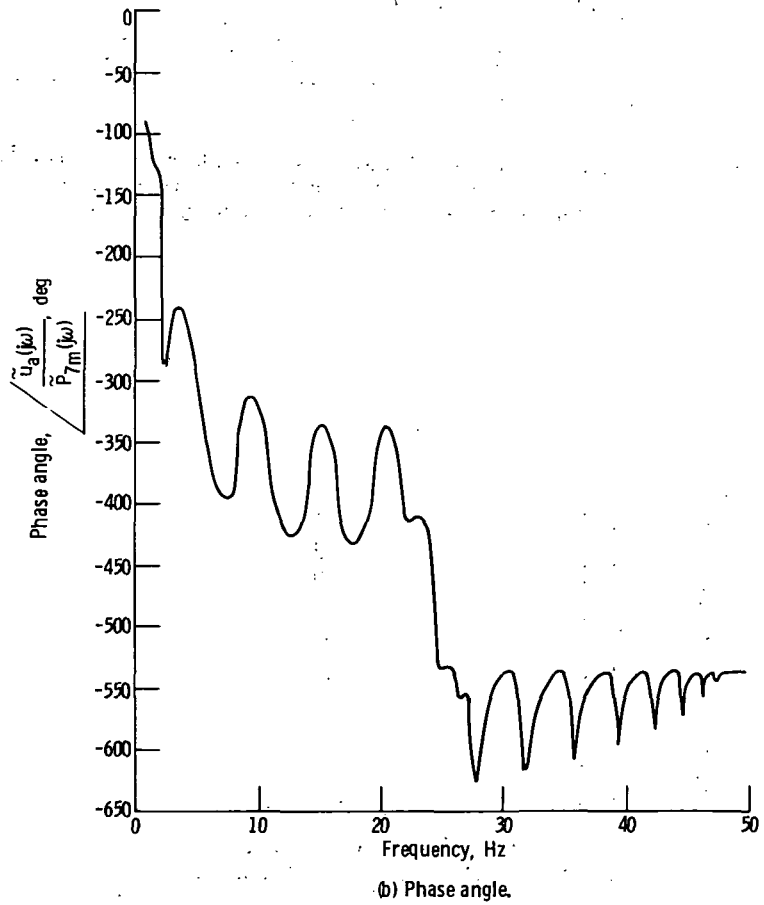
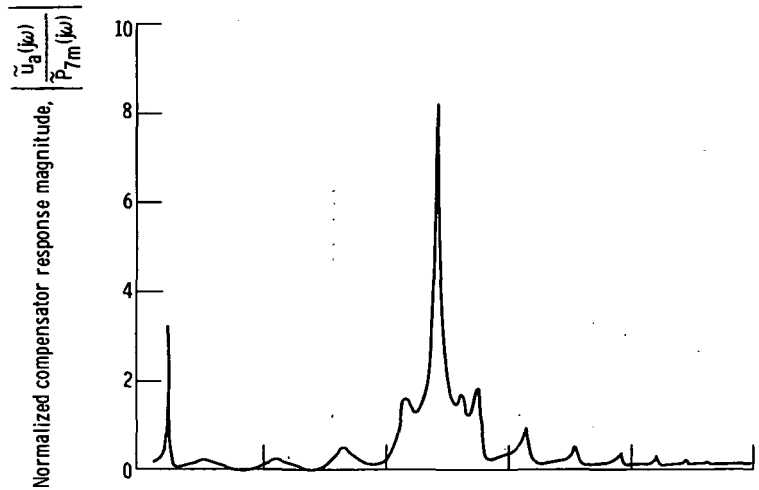


Figure 25. - Feedback compensator frequency response for modal control. Control weighting,  $r_2 = 1.0$ ; ratio of disturbance to measurement noise,  $\tilde{\psi}_w/\tilde{\psi}_v = 1.95$  (low measurement noise).

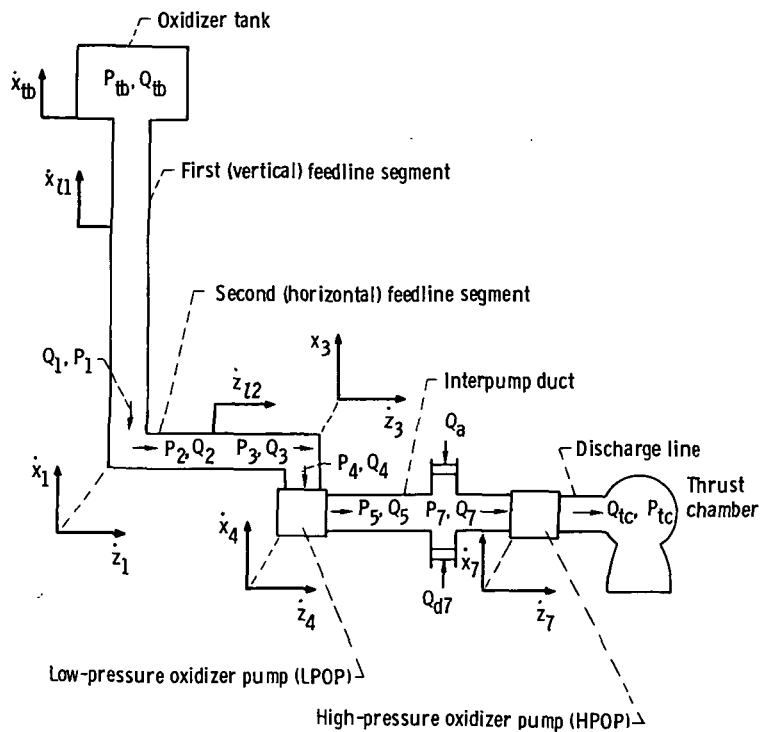


Figure 26. - Schematic of liquid-oxygen-system model.

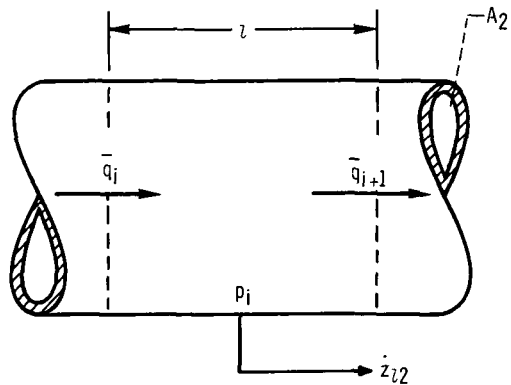


Figure 27. - Feedline control volume. Lump length,  $l$ ; pressure in  $i$ th lump (second feedline),  $p_i$ ; flow entering  $i$ th lump (second feedline),  $\bar{q}_i$ ; horizontal feedline velocity,  $\dot{z}_{12}$ ; cross-sectional area (second feedline),  $A_2$ .

1. Report No. NASA TP 1217	2. Government Accession No.	3. Recipient's Catalog No.	
4. Title and Subtitle SPACE SHUTTLE ACTIVE-POGO-SUPPRESSOR CONTROL DESIGN USING LINEAR QUADRATIC REGULATOR TECHNIQUES		5. Report Date January 1979	6. Performing Organization Code
		8. Performing Organization Report No. E-9578	
7. Author(s) Bruce Lehtinen and Carl F. Lorenzo		10. Work Unit No. 505-05	11. Contract or Grant No.
9. Performing Organization Name and Address National Aeronautics and Space Administration Lewis Research Center Cleveland, Ohio 44135		13. Type of Report and Period Covered Technical Paper	
		14. Sponsoring Agency Code	
12. Sponsoring Agency Name and Address National Aeronautics and Space Administration Washington, D.C. 20546		15. Supplementary Notes	
16. Abstract Two methods of active pogo suppression (stabilization) for the space shuttle vehicle were studied analytically. The basis for both approaches was the linear quadratic regulator, state space technique. The first approach minimized root-mean-square pump inlet pressure by using either full-state feedback, partial-state feedback, or output feedback with a Kalman filter. The second approach increased the modal damping associated with the critical structural modes by using either full-state feedback or reconstructed state feedback. A number of implementable controls were found by both approaches. The designs were analyzed with respect to sensitivity, complexity, and controller energy requirements, as well as controller performance. Practical controllers resulting from the two design approaches tended to use pressure and flow as feedback variables for the minimum-rms method and structural accelerations or velocities for the modal control method. Both approaches are suitable for the design of active pogo-suppression controllers.			
17. Key Words (Suggested by Author(s)) Space shuttles; Pogo; Optimal control; Feedback control; Kalman filters; Modal response; Eigenvalues; Structural vibration; Oscillations; Eigenvectors; Stabilization		18. Distribution Statement Unclassified - unlimited STAR Category 33	
19. Security Classif. (of this report) Unclassified	20. Security Classif. (of this page) Unclassified	21. No. of Pages 82	22. Price* A05

National Aeronautics and  
Space Administration

Washington, D.C.  
20546

Official Business

Penalty for Private Use, \$300

THIRD-CLASS BULK RATE

Postage and Fees Paid  
National Aeronautics and  
Space Administration  
NASA-451



**NASA**

POSTMASTER: If Undeliverable (Section 158  
Postal Manual) Do Not Return

---